

The Interplay Between Forces, Particle Rearrangements, and Macroscopic Stress Fluctuations in Sheared 2D Granular Media

Kwangmin Lee^a, Ryan C. Hurley^{a, b *}

^a *Department of Mechanical Engineering, Johns Hopkins University, Baltimore, Maryland 21218, USA*

^b *Hopkins Extreme Materials Institute, Johns Hopkins University, Baltimore, Maryland 21218, USA*

Abstract

Recent studies have established correlations between non-affine motion and macroscopic stress fluctuations in sheared granular media. However, a comprehensive examination of the relationship between non-affine motion, macroscopic stress fluctuations, and inter-particle forces remains lacking. We investigated this interplay in 2D granular media subjected to plane shear. We found that particle rearrangements originated from regions featuring the greatest instantaneous reduction of inter-particle forces. This “greatest reduction” (GR) region coincided with the location in which the maximal non-affine motion, as quantified by D^2_{\min} , first coalesced into a single connected region. The magnitude of the maximal non-affine motion correlated strongly with the magnitude of the macroscopic stress fluctuation. Furthermore, this correlation increased when particles in a larger neighborhood of the point of maximal non-affine motion were included in the calculation, suggesting that plastic events are best thought of not as point-like events but regional events. Our results held for various sliding coefficients and a variety of sample sizes. Our findings suggest that elastoplastic models should consider plastic events as regional rather than point-like.

Keywords: Particle rearrangement; Stick-slip behavior; Shear transformation zone; Differential Force network

* Corresponding author. Tel.: +1 410 516 5569

E-mail address: rhurley6@jhu.edu

1. Introduction

Plastic deformation has been extensively studied in granular materials because of the prevalence of these materials in industrial and geophysical processes, and in natural hazards such as earthquakes and landslides. Plasticity in granular and other disordered solids remain challenging to predict because the structure of these materials lacks long-range order. This lack of long-range order implies that defects which can act as nucleation sites for plasticity cannot be easily identified. In contrast, defects such as dislocations in crystalline materials are straightforward to identify and are closely related to the initiation and progression of plasticity.

There are broadly two approaches which have been taken to study plasticity in granular and amorphous materials: an approach which focuses on microscopic dynamics such as particle rearrangements and an approach which focuses on the inter-particle force network. Shear transformation zone (STZ) theories align primarily with the first approach. Argon, Spaepen, and others [1-3] inspired the concept of STZs by explaining plastic deformation in metallic glasses as thermally-activated shear transformations initiated around free volume regions. Falk and Langer [4] formally introduced the notion of STZs as local regions where rearrangements occur. To identify STZs, the same authors developed D^2_{\min} , which measures how local particle dynamics deviate from affine deformation. Langer [5] established an analytical mean-field elastoplastic model (EPM), introducing STZs as zones experiencing plastic deformation. In this model, a quadrupolar elastic displacement field is produced around an STZ, and a corresponding change in the local stress fields occurs. Picard *et al.* [6-7] advanced this model by introducing an EPM which considers the long-range elastic perturbation induced by a localized plastic event. Nicolas *et al.* [8] reviewed various other EPMs for granular and amorphous solids. None of these EPMs consider the effects of rearrangements on local structure, and all EPMs treat long-range elastic perturbations in an idealized manner. Zhang *et al.* [9] showed that softness, a machine-learned measure of local structure, is strongly correlated with the propensity of a local region to rearrange, emphasizing the importance of incorporating local structure into elastoplastic models. Finally, many studies have employed correlation analysis between macroscopic plasticity and various structural indicators to identify indicators which may be used to identify structural defects responsible for plastic flow in amorphous solids [10-18]. All prior studies focusing on microscopic dynamics and particle rearrangements provide a strong foundation upon which to understand macroscopic plasticity, but a stronger link to inter-particle force fluctuations is needed to understand the fully anisotropic and non-local nature of plastic events.

Taking the approach to plasticity based on inter-particle force networks, Cates *et al.* [19] proposed a simple model to explain the jamming to unjamming transition based on the now well-known concept of

force chain buckling. Tordesillas [22] examined unjamming transitions and associated instabilities and particle rearrangements in dense granular systems using discrete element method (DEM) simulations, identifying force chain buckling as a primary source of plastic events. Tordesillas and Muthuswamy [23] developed a multiscale thermo-micromechanical continuum model of dense granular materials considering force chain buckling. Tordesillas and Muthuswamy [24] established an analytical model for force chain buckling and performed a parametric study to determine the effect of particle-scale properties on force chain stability. Using force chains and minimal contact cycles, Tordesillas *et al.* [25] studied the evolving stability of jammed states of specific cluster conformations, *i.e.*, particles forming force chains and minimal contact cycles in dense granular materials. Kramer *et al.* [26] and Bretz *et al.* [27] found that by using the average of local measures, including the persistence diagram of force network, the differential force network (which quantifies changes in the magnitude of inter-particle forces over a given time interval), and measures of broken, mobile, and nonmobile contacts, the time to macroscale slip could be predicted. Gupta *et al.* [28] studied force chain behavior occurring during macroscopic stress fluctuations and found that force chains may either buckle or remain stable during macroscopic stress drops depending on the behavior of the surrounding weak force network.

Although the two approaches of analyzing microscopic dynamics and force networks are complementary, studies connecting the concepts of local rearrangements (non-affine motion), macroscopic stress fluctuations, and changes in inter-particle forces remains limited. Examples of such studies include one by Ma *et al.* [29], who examined the initialization and localization of plastic events on various timescales in sheared granular media. They found a moderate correlation between the magnitude of D^2_{\min} and local stress fluctuations, indicating that non-affine motion originated at particles experiencing significant stress fluctuations over short time scales. Ma *et al.* [30] and Mei *et al.* [31-32] predicted macroscale stress fluctuations based on the D^2_{\min} field using machine learning. They found that, during stress drop events, regions of elevated D^2_{\min} are spatially concentrated and tend to generate large clusters inside the granular system. However, many fundamental questions remain unresolved, including what type of spatial information is important for the predictions of macroscopic response, whether there are some mesoscopic structures responsible for varying macroscopic responses, and what causes the different spatial patterns of mesoscopic structures [32].

The primary goals of this work are to do the following in 2D sheared granular media: (1) establish links between local non-affine motion and local changes in the inter-particle force network; (2) establish links between microscopic dynamics and macroscopic stress fluctuations. We employed 2D DEM simulations of granular materials subjected to plane shear. We found that the region featuring the largest instantaneous

drop in inter-particle force magnitudes, referred to as the greatest reduction (GR) region, was subsequently the location of the largest D_{\min}^2 . The emergence of a single clustered GR region and the maximal D_{\min}^2 value also coincided with the onset of a macroscopic stress fluctuation. Furthermore, the magnitude of D_{\min}^2 in the GR region correlated strongly with the magnitude of the macroscopic stress fluctuation, particularly for large stress drops. We expect that our research will contribute to the understanding of particle rearrangements and aid in developing an EPM in granular materials.

The remainder of the paper is structured as follows. Section 2 introduces the DEM model used for plane shear simulations. Section 3.1 discusses the macroscale DEM results for a small sample containing around 1,000 particles. The relationship between the microscopic dynamics and the differential force network for this sample is analyzed in detail in Section 3.2. Section 3.3 provides a correlation analysis between the macroscale response and various kinematic measures. Section 3.4 discusses the expansion of DEM simulations to other sliding friction coefficients and samples with a larger number of particles, containing many thousands of particles. Section 4 offers a discussion, and Section 5 provides concluding remarks.

2. Discrete Element Method (DEM) Model

We created two-dimensional DEM models of a plane shear test (Fig. 1) in the open-source code LIGGGHTS, version 3.8.0 [33]. We used a uniform distribution of particle radius between 0.5-1 μm . The number of particles in the simulations discussed in the main text was approximately 1,000, but we confirmed our findings with simulations containing approximately 5,000 particles and we report the results of those simulations in the Supplemental Materials [34]. For boundary conditions, the particles constituting the bottom wall were fixed, while particles constituting the upper wall were constrained to move together. The positions of particles constituting the bottom wall were integrated using a velocity-Verlet scheme to maintain a constant normal force, N . Their horizontal velocity, V , was held at a constant value to ensure that the sample was flowing in the quasi-static regime with an inertial number, I , of 4×10^{-6} [35]. The mass of the top wall used in the velocity-Verlet scheme was chosen to be the sum of the masses of the particles that constituted it. Particles between the top and bottom walls constituted the sample and were integrated using a velocity-Verlet scheme, and gravity was neglected in all calculations. The sample's normal force, N , and shear force, S , are the sum of the normal and shear forces, respectively, acting on the particles constituting the top wall. We chose 10,000 for the contact stiffness number, κ , and thus simulations were in the elastic and stiff-particle regime in which particle stiffness does not qualitatively influence results [35]. For the normal and tangential contact models, the Hertzian contact model for cylindrical bodies [36] and Lai *et al.*'s semi-analytical Hertzian frictional model in two dimensions [37] were used, respectively, both

incorporating the linear damping models [38]. For the rolling resistance model, the type C elastic-plastic spring-dashpot model [39] was employed. Appendix A provides a detailed description of the contact models. For materials properties, 1 GPa, 0.2, 0.9, and 2500 kg / m³ were chosen for Young's modulus, Poisson's ratio, coefficient of restitution, and density, respectively. For the sliding friction coefficient, μ_s , and the rolling friction coefficient, μ_r , 0.7 and 0.01 were used, respectively. Here, we assumed that the particle shape was circular and the actual contact moment was negligible, and thus a small value was chosen for μ_r . The contact moment introduced in this DEM model is an artificial means of capturing the effect of particle shape irregularities. The simulations for various μ_s were also conducted and the results are given in Section 3.4 and the Supplemental Material [34]. Varying μ_s did not qualitatively change our results. For damping constants at the contact, 0.1, 0.1, and 0.3 were chosen for viscoelastic damping constant for normal force, γ_n , viscoelastic damping constant for tangential force, γ_t , and rolling viscous damping ratio, η_r , respectively.

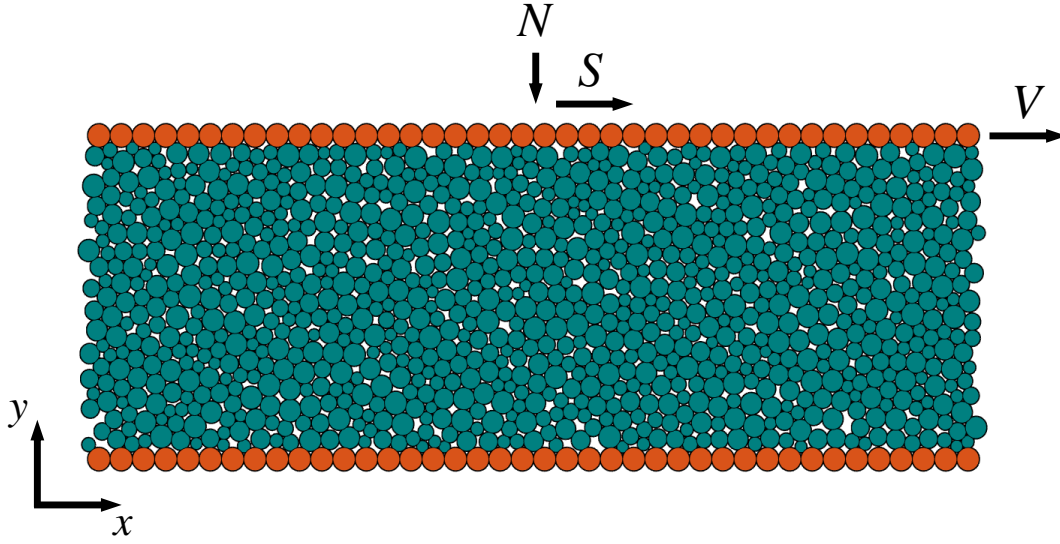


Fig. 1. DEM model for a plane shear test.

3. DEM Results

3.1. Macroscopic response

The normalized shear stress-strain curve is shown in Fig. 2a. The normalized shear stress, τ , is defined as the ratio of shear to normal force, S / N , measured in the sheared granular material, as described in Section 2.

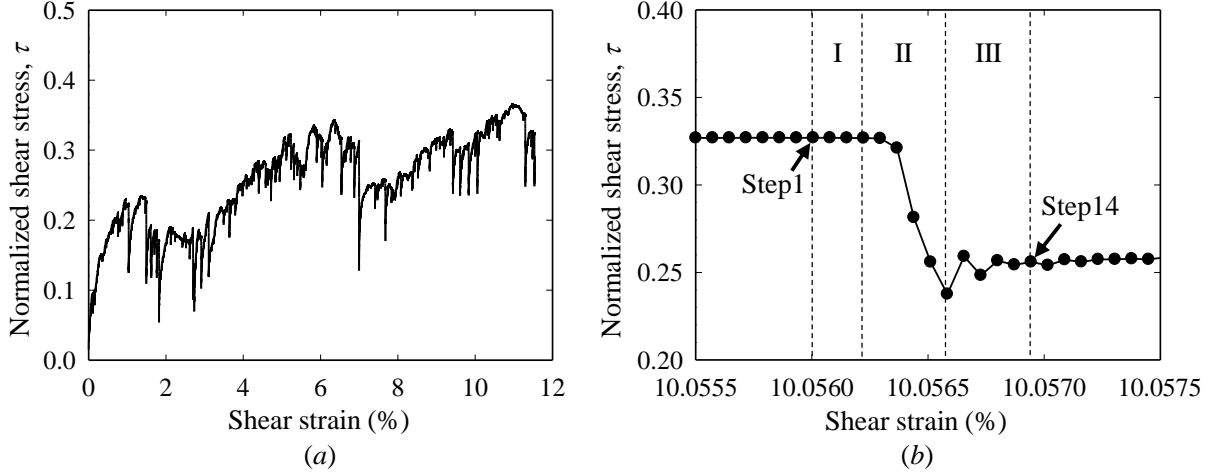


Fig. 2: (a) Normalized shear stress-strain curve from discrete element method simulation. (b) Normalized shear stress-strain curve around a slip event occurring between 10.0555% to 10.0575% shear strain; the region around the slip event is delineated into three distinct stages: the pre-stress drop stage (Stage I), the stress drop stage (Stage II), and the post-stress drop stage (Stage III).

3.2. Microscopic dynamics and differential force network analysis around a slip event

We focused our analysis of microscopic dynamics and force fluctuations on events occurring after 2.2% macroscopic shear strain. We refer to this portion of the simulation as the stick-slip regime. In the stick-slip regime, we observed a total of approximately 42,000 stick and slip events, which we collectively refer to as phases. A stick event (or phase) begins when τ increases and ends when this increase stops. A slip event (or phase) begins when τ decreases and ends when this decrease stops. We note that while a macroscopic shear strain of 2.2% does appear to coincide with the onset of a critical state in Fig. 2a, the choice to analyze this regime permits analysis of many phases and leads to qualitatively similar results to analysis of phases in the critical state regime of the simulations with a larger number of particles, as shown in the Supplemental Material [34].

To gain insight into the nature of stick and slip events, we first focused on the largest stress drop observed in the stick-slip regime, specifically between 10.0555% to 10.0575% shear strain (see Fig. 2b). We analyze the statistics of all stick and slip events in subsequent subsections. We divided the slip event occurring between 10.0555% to 10.0575% shear strain into three stages based on the macroscale shear stress profile: pre-stress drop (Stage I), which is the period before the significant stress reduction begins; stress drop (Stage II), characterized by the largest decrease in stress; post-stress drop (Stage III), which is the period immediately following the stress drop stage. We studied these stages at the particle scale by examining the differential force network, the D^2_{\min} field, and the non-affine displacement field. The macroscale shear strain

increments between which inter-particle forces and particle positions were output from the DEM simulation, $\Delta\gamma$, was 7.2×10^{-7} for this analysis.

Figure 3 shows the particles experiencing the greatest 1% reduction in inter-particle force magnitude, the differential force network, the particles experiencing the greatest 1% D^2_{\min} , and the full D^2_{\min} field at each $\Delta\gamma$ increment in Stages I-III of the stress drop occurring between 10.0555 - 10.0575% shear strain. The step numbers in Fig. 3 are noted in Fig. 2b. The differential force network was calculated as $f^\alpha_t - f^\alpha_{t-1}$ of each contact α , where f^α_t and f^α_{t-1} are the magnitudes of inter-particle force vectors at the current time step and previous time step (separated by a strain increment of 7.2×10^{-7}), respectively. If force-bearing contacts at the previous time step are created or destroyed at a given time step, the differential force network at this contact is zero in the current time step. D^2_{\min} was computed based on the definition in [32] with a local averaging region of radius $r = 5r_p$, where r_p is the average radius of particles. The details of the D^2_{\min} computation can be found in Appendix B. In theory, an STZ can be considered a local plastic event; on the other hand, a group of rattler particles undergoing a change in configuration may be identified as an STZ using D^2_{\min} . We define rattler particles as particles inside the sample that have two or fewer inter-particle contacts, and particles in the top or bottom walls that have one or fewer inter-particle contacts. Because these rattler particles are not involved in stress transmission during a plastic event, they were excluded from the computation of D^2_{\min} . The colorless disks in the D^2_{\min} graphs in the right-most column of Figure 3 represent the rattler particles.

Before the stress drop occurred, in Stage I, both the differential forces and D^2_{\min} were somewhat randomly distributed spatially, although initial signs of concentration towards a single region were already observed (Fig. 3). At the beginning of Stage II, the locations of the most-negative differential force concentrated towards a single region in the right lower portion of the sample and formed a single cluster (Step 4) (Fig. 3). To further examine this phenomenon, we introduce the concept of a GR region, which refers to a set of particles that experience the top 1% reduction in inter-particle force magnitudes. A single clustered GR region was first established at Step 4. Locations with high D^2_{\min} values also concentrated towards a single region in the right lower part of the sample and formed a single cluster at the beginning of Stage II (Step 4) (Fig. 3). This single clustered region of elevated D^2_{\min} coincided with the GR region. In this instance, we therefore conclude that the particle rearrangement likely originated from the weakening of the single clustered GR region.

From Step 6 of this stress drop event, the single clustered GR region no longer existed, likely due to force chain collapse. Figure 3 shows that, from Step 6 to Step 8, the differential force change propagated away from the location where the single clustered GR region had first been established. In addition, the D^2_{\min}

distribution in Steps 6-8 shows that particle rearrangements continued occurring at the location where the single clustered GR region was first established in Step 4 (Fig. 3). Thus, the elimination of the single clustered GR cluster, potentially through force chain collapse, likely caused both the differential force change propagation and particle rearrangement propagation.

In any contact points other than those in the GR region, inter-particle force change was almost zero during Steps 4-6 (Fig. 3). Thus, a macroscale stress drop appears to occur due to a significant inter-particle force decrease in the GR region and the subsequent structural change in the sample. In Stage III, differential force changes and the propagation of particle rearrangements ended. Figure 3 shows that differential forces and D^2_{\min} were randomly distributed during Stage III.

Figure 4 illustrates the non-affine displacement field during Stages I-III. There was a distinct region of concentrated non-affine displacement at each of Steps 5-6. This region coincided with the single clustered region of high D^2_{\min} in Figure 3. During these steps, the non-affine displacement field was qualitatively seen to exhibit quadrupolar symmetry, consistent with observations made in previous studies for amorphous materials [40-41].

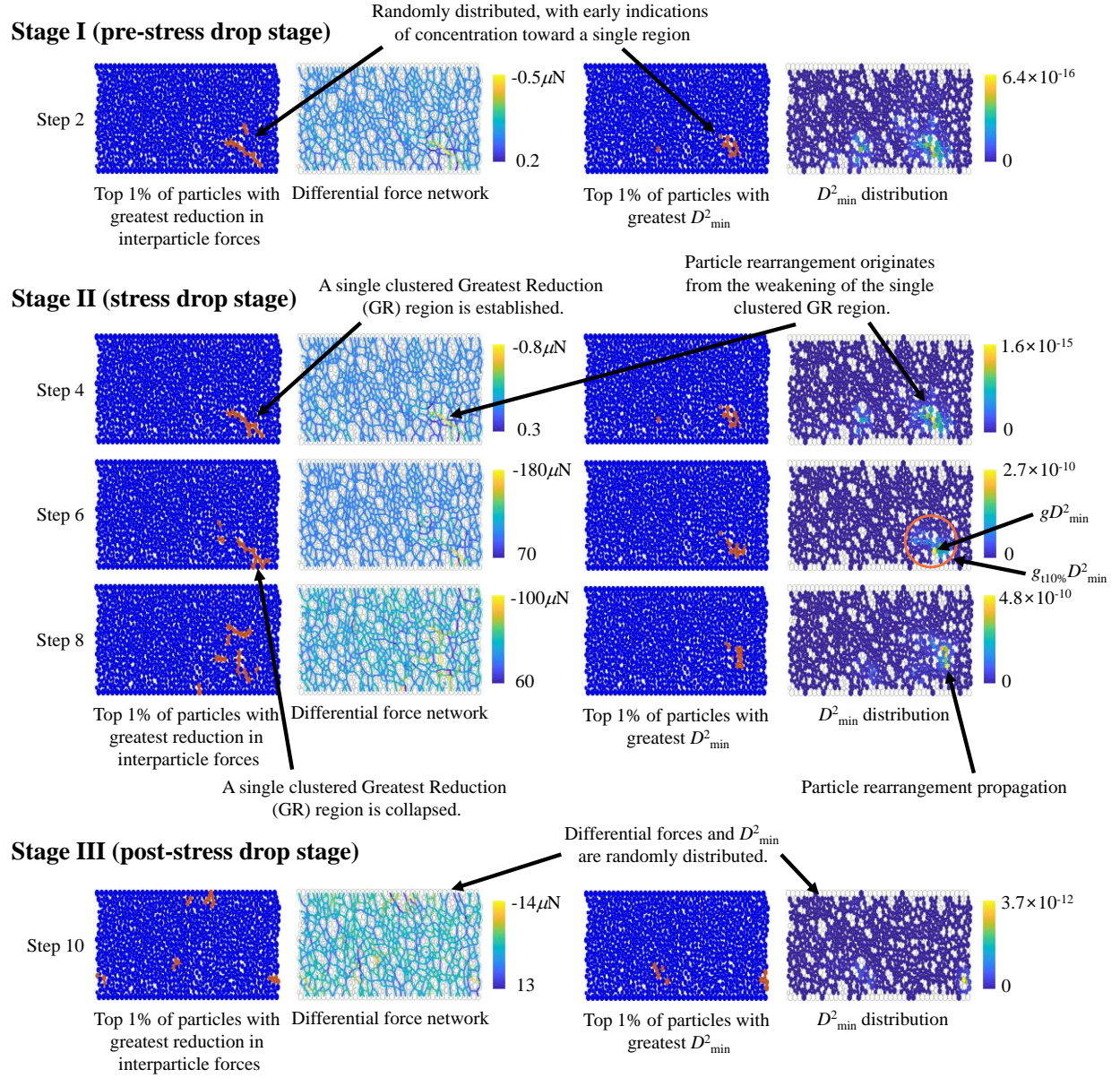


Fig. 3. Particles with the top 1% reduction in inter-particle force magnitude, differential force network, particles with greatest 1% of D^2_{\min} , and the D^2_{\min} field at each $\Delta\gamma$ increment in Stages I-III. Results are shown for selected even-numbered time steps to enhance clarity and understanding of particle rearrangements. The location of particles for gD^2_{\min} and $g_{t10\%}D^2_{\min}$ for Step 6 are indicated in D^2_{\min} distribution field.

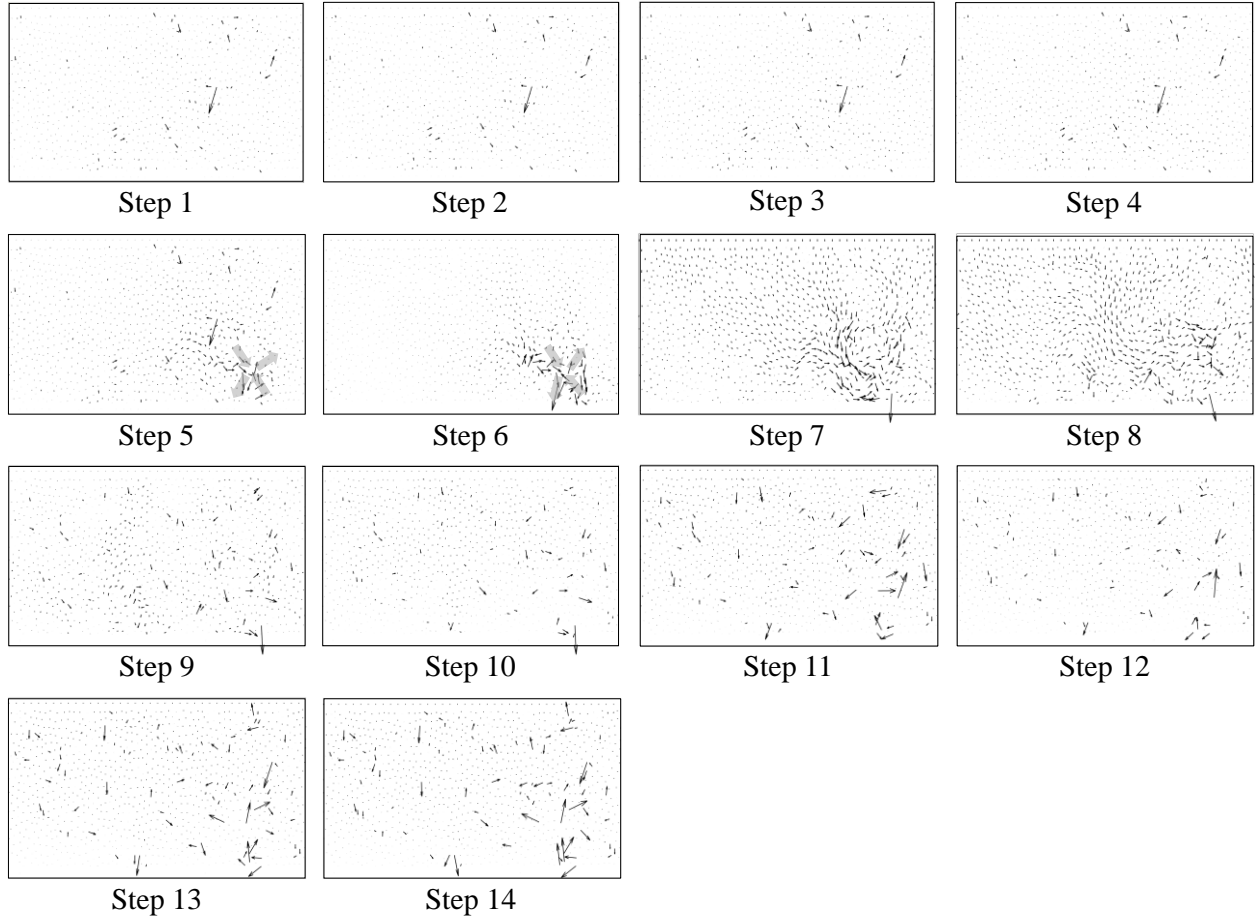


Fig. 4. Non-affine displacement field around the slip event. The arrows represent the displacement vectors, with the length of each arrow indicating its relative magnitude. Note that the arrow lengths are scaled differently for each step to highlight relative displacements. The gray arrows in Steps 5-6 indicate tension and compression directions.

The Spearman correlation coefficients between the absolute values of the maximum principal stress changes, $|\Delta\sigma_p|$, and D^2_{\min} of each particle during the 10.0555 - 10.0575% sample shear strain are shown in Figure 5a. This curve shows that the correlation between $|\Delta\sigma_p|$ and D^2_{\min} was high during Steps 4-5, as particle rearrangement was primarily driven by the weakening of the single clustered GR region. However, from Step 6 in Stage II, the correlation between $|\Delta\sigma_p|$ and D^2_{\min} became weak because the single clustered GR region collapsed and particle rearrangements propagated outward from the region.

Figure 5b illustrates the greatest D^2_{\min} value, denoted as gD^2_{\min} , and the average of the greatest 10% D^2_{\min} values, denoted as $g_{t10\%}D^2_{\min}$, within the sample across each timestep during 10.0555 - 10.0575% sample shear strain. Defining a stable structure as one in which particle rearrangement does not occur, the sample

exhibited stability in Stage I marked by low gD_{\min}^2 values. At the onset of Stage II, we observed an increase in gD_{\min}^2 , which signifies the beginning of an instability. In Stage III, gD_{\min}^2 gradually decreased, indicating a return toward stability. However, the normalized shear stress-strain curve continued to fluctuate over short time periods in Stage III (Fig. 2b). The $g_{t10\%}D_{\min}^2$ shows the same trend with gD_{\min}^2 during the 10.0555 - 10.0575% sample shear strain, with slightly lower values.

Figure 5c illustrates the number of clusters in the GR region during the 10.0555 - 10.0575% sample shear strain. To identify and differentiate these clusters, the DBSCAN (Density-Based Spatial Clustering of Applications with Noise) algorithm was employed in MATLAB R2020a [42]. The algorithm was applied to the positions of particles exhibiting the greatest 1% reduction in inter-particle force. The parameter set for each cluster included a neighborhood search radius of $r = 5r_p$ and a minimum requirement of 1 neighbor for a point to be considered a core point. Initially, in Stage I, the clusters in the GR region were multiple and spatially dispersed (Fig. 3). At the onset of Stage II, they converged into a single cluster before dispersing once again in Stage III (Fig. 3). The number of clusters in the GR region therefore fluctuated in Stage III (Fig. 5c).

Figure 5d shows the average and median of the absolute values of the contact angles in the GR region during the 10.0555 - 10.0575% sample shear strain. The contact angle at a contact point α , θ_α , is defined as an angle (in radians) between the x -axis and an inter-particle force vector. Both the average and median of the absolute values of contact angles in the GR region fluctuated significantly from Stage II, indicating no discernible trends once particle rearrangement started to occur.

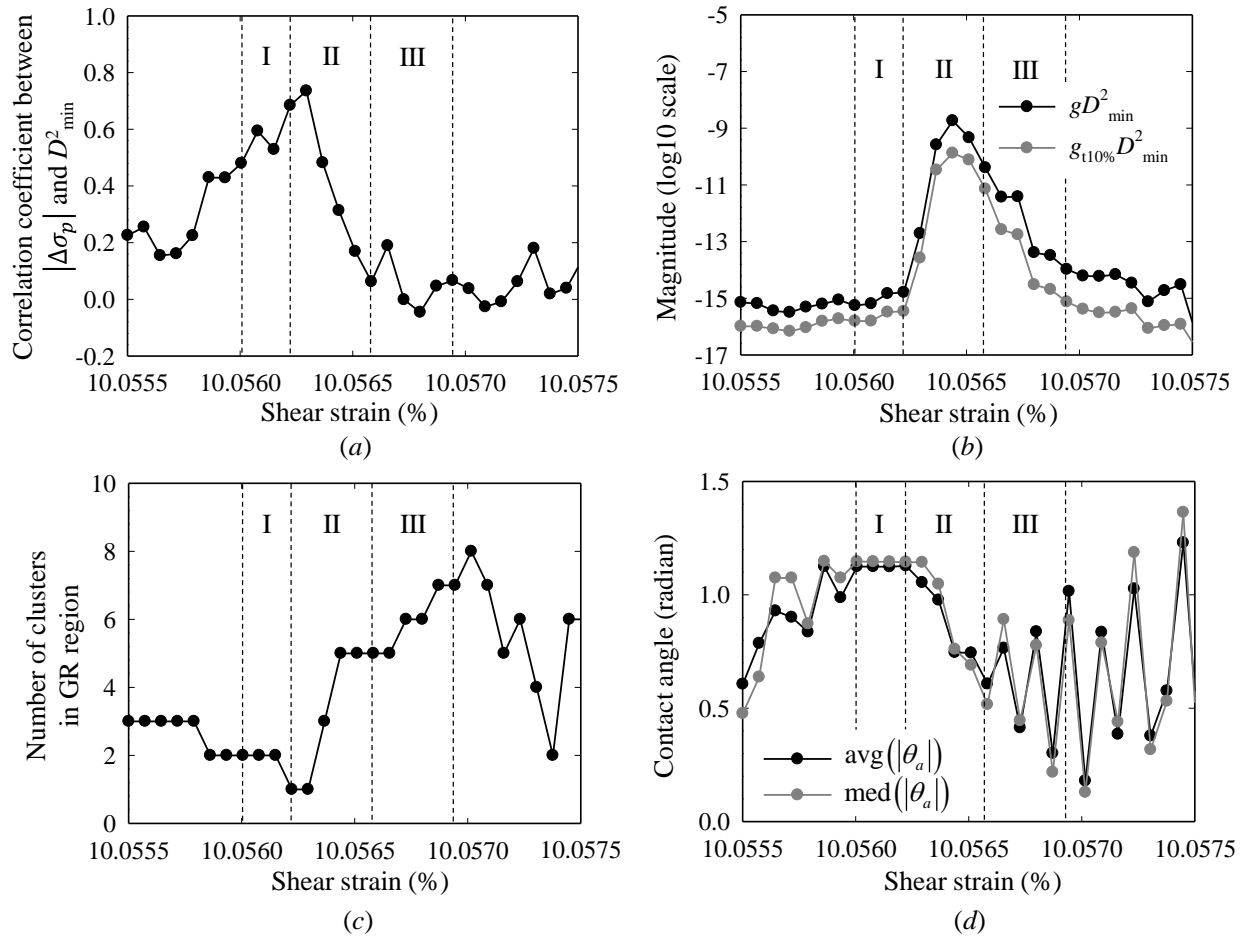


Fig. 5. (a) The Spearman correlation coefficients between the absolute values of maximum principal stress change, $|\Delta\sigma_p|$, and D_{\min}^2 at particles, (b) the greatest D_{\min}^2 and the average of greatest top 10% D_{\min}^2 magnitudes, (c) the number of clusters in the GR region, and (d) the average and the median of the absolute values of the contact angles in the GR region during 10.0555 to 10.0575% sample shear strain.

3.3. Correlation analysis for all stress fluctuations

In this section, we build upon the initial observations noted for a single stress drop event in Section 3.2 and statistically analyze the results of the entire DEM simulation. Using the data from approximately 130,000 timesteps and 42,000 observed stick and slip events (phases) for shear strain $\geq 2.2\%$, we investigated correlations between microscopic responses and stress fluctuations, $\Delta\tau$.

In Section 3.2, we discovered that for the studied stress drop, particles experiencing the greatest reduction in inter-particle forces were spatially clustered and particle rearrangements originated from this region. Accordingly, a single particle with the greatest D_{\min}^2 value in a local region of a sample may determine the

overall particle rearrangement behavior. Thus, gD_{\min}^2 emerged as a parameter to correlate against $\Delta\tau$ for all timesteps of interest. On the other hand, the single particle with the greatest D_{\min}^2 value may induce shear transformations in neighboring zones, depending on the surrounding structures. Therefore, $g_{t10\%}D_{\min}^2$ also emerged as a parameter to correlate against $\Delta\tau$ for all timesteps of interest. Figure 6a illustrates the absolute values of the Spearman correlation coefficients between instantaneous values of $\Delta\tau$ and both gD_{\min}^2 and $g_{t10\%}D_{\min}^2$ across all timesteps for shear strain $\geq 2.2\%$. We omit correlation coefficient data from all figures in this paper where the P -value exceeds 0.05, ensuring that only statistically significant results are presented. The analysis revealed that $\Delta\tau$ is weakly correlated with both gD_{\min}^2 and $g_{t10\%}D_{\min}^2$ (correlation less than 0.4) when $\Delta\tau$ decreases with a small magnitude ($-10^{-3} < \Delta\tau < -10^{-4}$), and moderately correlated (correlation between approximately 0.4 and 0.6) at values of $\Delta\tau$ with larger magnitude ($-10^{-1} < \Delta\tau < -10^{-2}$). Conversely, when $\Delta\tau$ increases significantly ($10^{-3} < \Delta\tau < 10^{-2}$), the correlation with both parameters is moderate.

Although $\Delta\tau$ shows a weak to moderate correlation with both gD_{\min}^2 and $g_{t10\%}D_{\min}^2$ when it decreases considerably within the range of -10^{-1} to -10^{-2} , Figures 2b and 5b show that $\Delta\tau$ lags behind the increase of gD_{\min}^2 and $g_{t10\%}D_{\min}^2$. Consequently, instead of correlating $\Delta\tau$ with instantaneous values of gD_{\min}^2 or $g_{t10\%}D_{\min}^2$ across all timesteps, we assessed the correlation between $\Delta\tau_p$, defined as the change of normalized shear stress from the start to the end of a phase (stick or slip event), and four parameters. The first parameter is the peak value of gD_{\min}^2 observed in a sample during a stick or slip event (Equation 1). The second examines the peak value of $g_{t10\%}D_{\min}^2$ observed in a sample during a stick or slip event (Equation 2). The third is the sum of the gD_{\min}^2 values within an event (Equation 3), starting from t_s , the initial timestep when the clusters of GR region are at their minimum, to t_e , the concluding timestep of the stick or slip event. The fourth parameter is the sum of the $g_{t10\%}D_{\min}^2$ values within a phase (Equation 4), starting from t_s to t_e . Mathematically, these parameters are given by:

$$mgD_{\min}^2 = \max_{\text{phase}}(gD_{\min}^2) \quad (1)$$

$$mg_{t10\%}D_{\min}^2 = \max_{\text{phase}}(g_{t10\%}D_{\min}^2) \quad (2)$$

$$sgD_{\min}^2 = \sum_{t=t_s}^{t_e} gD_{\min}^2 \quad (3)$$

$$sg_{t10\%}D_{\min}^2 = \sum_{t=t_s}^{t_e} g_{t10\%}D_{\min}^2 \quad (4)$$

Figure 6b illustrates the absolute values of the Spearman correlation coefficients between $\Delta\tau_p$ and mgD_{\min}^2 , $mg_{t10\%}D_{\min}^2$, sgD_{\min}^2 , and $sg_{t10\%}D_{\min}^2$ for stick and slip events for shear strain $\geq 2.2\%$. For $-10^{-1} <$

$\Delta\tau_p < -10^{-3}$, the correlations between $\Delta\tau_p$ and all four parameters show stronger associations compared to those of $\Delta\tau$ with gD_{\min}^2 and $g_{t10\%}D_{\min}^2$ across all timesteps ($-10^{-1} < \Delta\tau < -10^{-3}$) (see Fig. 6a-b). This greater correlation observed for all phases, rather than across all individual timesteps, suggests that the microscopic dynamics throughout the duration of stick and slip events is more closely linked to macroscale plasticity. The results show that the correlation between $\Delta\tau_p$ and sgD_{\min}^2 and between $\Delta\tau_p$ and mgD_{\min}^2 exhibit similar trends, both indicating a moderate to strong correlation (above 0.6) within the range of $-10^{-1} < \Delta\tau_p < -10^{-3}$. This also suggests that instead of analyzing particle dynamics throughout the entire phase, it is sufficient to focus on the points within the phase where the most pronounced non-affine motion occurs. The correlation between $\Delta\tau_p$ and $mg_{t10\%}D_{\min}^2$ and between $\Delta\tau_p$ and $sg_{t10\%}D_{\min}^2$ demonstrates a slightly stronger correlation than the other parameters in the same $\Delta\tau_p$ range. This suggests that the variability in the D_{\min}^2 values of the particles surrounding the particle with gD_{\min}^2 affects $\Delta\tau_p$, supporting the notion that rearrangement events should be interpreted as non-local, regional phenomena, not point-like phenomena.

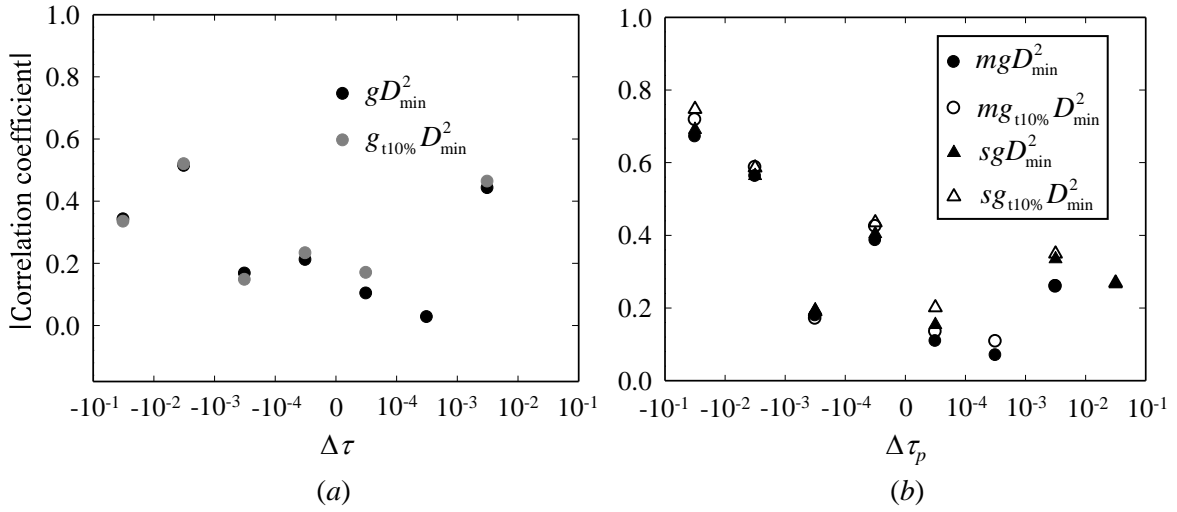


Fig. 6. (a) Graphs of the absolute values of the Spearman correlation coefficients between $\Delta\tau$ and gD_{\min}^2 and between $\Delta\tau$ and $g_{t10\%}D_{\min}^2$ across all timesteps for shear strain $\geq 2.2\%$, and (b) graphs of the absolute values of the Spearman correlation coefficients between $\Delta\tau_p$ and mgD_{\min}^2 , $mg_{t10\%}D_{\min}^2$, sgD_{\min}^2 , and $sg_{t10\%}D_{\min}^2$ for all stick and slip events for shear strain $\geq 2.2\%$.

Under the hypothesis that the duration of phases affected correlations with microscopic parameters, we further analyzed the Spearman correlation coefficients between $\Delta\tau_p$ and mgD_{\min}^2 , $mg_{t10\%}D_{\min}^2$, sgD_{\min}^2 , and $sg_{t10\%}D_{\min}^2$ for phases with duration, t_p , longer than $3\Delta\gamma$ (called long, or l) and for phases shorter than or equal to $3\Delta\gamma$ (called short, or s). Figure 7a-b show these correlation coefficients. The results indicate that the correlations between $\Delta\tau_p$ and mgD_{\min}^2 , $mg_{t10\%}D_{\min}^2$, sgD_{\min}^2 , and $sg_{t10\%}D_{\min}^2$ in long phases not only follow the same trend as those observed in all phases but are also stronger, particularly when $-10^{-1} < \Delta\tau_p < -10^{-4}$ (Figs. 6b and 7a). Among correlated variables, correlations between $\Delta\tau_p$ and $mg_{t10\%}D_{\min}^2$ and between $\Delta\tau_p$ and $sg_{t10\%}D_{\min}^2$ were stronger than correlations between $\Delta\tau_p$ and mgD_{\min}^2 and between $\Delta\tau_p$ and sgD_{\min}^2 in long phases during the slip events ($\Delta\tau_p < 0$). This indicates that D_{\min}^2 values of the particles surrounding the particle with gD_{\min}^2 influences $\Delta\tau$ in long slip events, again suggesting that these long slip events are regional rather than point-like phenomena. During slip events ($\Delta\tau_p < 0$), the correlations between $\Delta\tau_p$ and $sg_{t10\%}D_{\min}^2$ are stronger than those between $\Delta\tau_p$ and $mg_{t10\%}D_{\min}^2$ in long phases, further indicating history-dependence, as $sg_{t10\%}D_{\min}^2$ reflects the full history of particle rearrangements during a slip event. In addition, during slip events ($\Delta\tau_p < 0$), the correlations between $\Delta\tau_p$ and both $mg_{t10\%}D_{\min}^2$ and $sg_{t10\%}D_{\min}^2$ for long phases are strong for larger events ($\Delta\tau_p < -10^{-2}$) and mostly moderate for smaller events ($10^{-2} < \Delta\tau_p < 0$). The correlations between $\Delta\tau_p$ and mgD_{\min}^2 , $mg_{t10\%}D_{\min}^2$, sgD_{\min}^2 , and $sg_{t10\%}D_{\min}^2$ in short phases are significantly weaker than those in long phases when $-10^{-1} < \Delta\tau_p < -10^{-4}$.

To study the effect of the dynamics of neighboring particles around the particle with gD_{\min}^2 , excluding the influence of the particle with gD_{\min}^2 itself, we measured the Spearman partial correlation coefficient between $\Delta\tau_p$ and $mg_{t10\%}D_{\min}^2$ for long phases. The Spearman partial correlation coefficient between $\Delta\tau_p$ and $mg_{t10\%}D_{\min}^2$, excluding the effect of gD_{\min}^2 , was calculated as [43]:

$$\rho_{\Delta\tau_p, mg_{t10\%}D_{\min}^2 | gD_{\min}^2} = \frac{\rho_{\Delta\tau_p, mg_{t10\%}D_{\min}^2} - \rho_{\Delta\tau_p, gD_{\min}^2} \cdot \rho_{gD_{\min}^2, mg_{t10\%}D_{\min}^2}}{\sqrt{1 - \rho_{\Delta\tau_p, gD_{\min}^2}^2} \sqrt{1 - \rho_{gD_{\min}^2, mg_{t10\%}D_{\min}^2}^2}} \quad (5)$$

where $\rho_{\Delta\tau_p, mg_{t10\%}D_{\min}^2}$ is the Spearman correlation coefficient between $\Delta\tau_p$ and $mg_{t10\%}D_{\min}^2$, $\rho_{\Delta\tau_p, gD_{\min}^2}$ is the Spearman correlation coefficient between $\Delta\tau_p$ and gD_{\min}^2 , and $\rho_{gD_{\min}^2, mg_{t10\%}D_{\min}^2}$ is the Spearman correlation coefficient between gD_{\min}^2 and $mg_{t10\%}D_{\min}^2$. Even though gD_{\min}^2 and $mg_{t10\%}D_{\min}^2$ generally follow the same trend during a slip event as shown in Figure 5b, time steps at which mgD_{\min}^2 and $mg_{t10\%}D_{\min}^2$ are measured can be slightly different within a phase. Thus, when calculating the partial correlation coefficient in Eq. (5), we used the gD_{\min}^2 value at the time step where $mg_{t10\%}D_{\min}^2$ is at its maximum in a phase. Figure 7c shows

these partial correlation coefficients. The results indicate that the partial correlations between $\Delta\tau_p$ and $mg_{t10\%}D_{\min}^2$ for long phases are mostly moderate for larger events ($\Delta\tau_p < -10^{-2}$). This finding also supports our previous argument that these long slip events are regional rather than point-like phenomena.

Figure 7d shows the Spearman correlation coefficients between $\Delta\tau_p$ and t_p for long and short events. The results show that $\Delta\tau_p$ and t_p are moderately correlated for large stick events ($\Delta\tau_p > 10^{-4}$). Unlike in slip events, the structure of a sample during stick events is stable and features small gD_{\min}^2 values, and thus τ_p increases slowly as t_p increases. On the other hand, particle rearrangement is dominant for the long slip events. Thus, $\Delta\tau_p$ and t_p are weakly correlated for the long slip events ($\Delta\tau_p < 0$). In short phases, $\Delta\tau_p$ and t_p shows a weak correlation.

Figure 8a-b shows the Spearman correlation coefficients between $\Delta\tau_p$ and both the average and median of the absolute contact angles in the GR region across various ranges of $mg_{t10\%}D_{\min}^2$ and $sg_{t10\%}D_{\min}^2$, respectively, during long stick and slip phases. These values were calculated at the last timestep when the number of clusters in the GR region is at its minimum within each phase. The results indicate weak correlations or correlations lacking statistical significance ($P\text{-value} > 0.05$), suggesting that the contact structure of the single clustered GR region does not influence $\Delta\tau_p$. This observation is attributed to the substantial fluctuations in the mean and median of the contact angles following the collapse of the single clustered GR region, as illustrated in Fig. 5d.

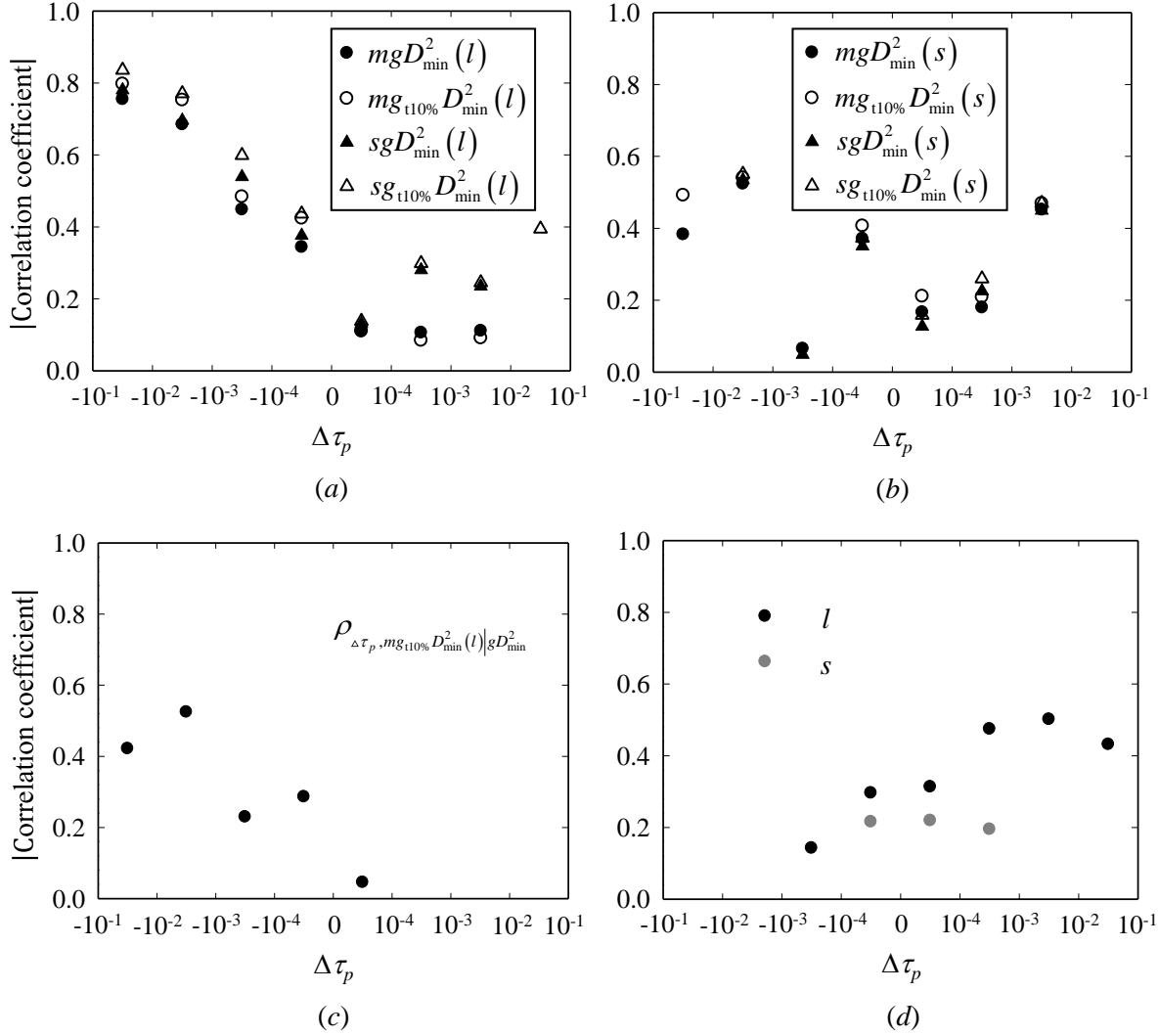


Fig. 7. Graphs of the absolute values of the Spearman correlation coefficients for $\Delta\tau_p$ with mgD_{\min}^2 , $mg_{t10\%}D_{\min}^2$, sgD_{\min}^2 , and $sg_{t10\%}D_{\min}^2$ for (a) long, l , ($> 3\Delta\gamma$) phases and (b) short, s , ($\leq 3\Delta\gamma$) phases in the stick-slip regime, (c) graph of the absolute values of the Spearman partial correlation coefficients for $\Delta\tau_p$ with $mg_{t10\%}D_{\min}^2$ excluding the effect of gD_{\min}^2 for long phases and (d) graphs of Spearman correlation coefficient for $\Delta\tau_p - t_p$ for long and short phases in the stick-slip regime.

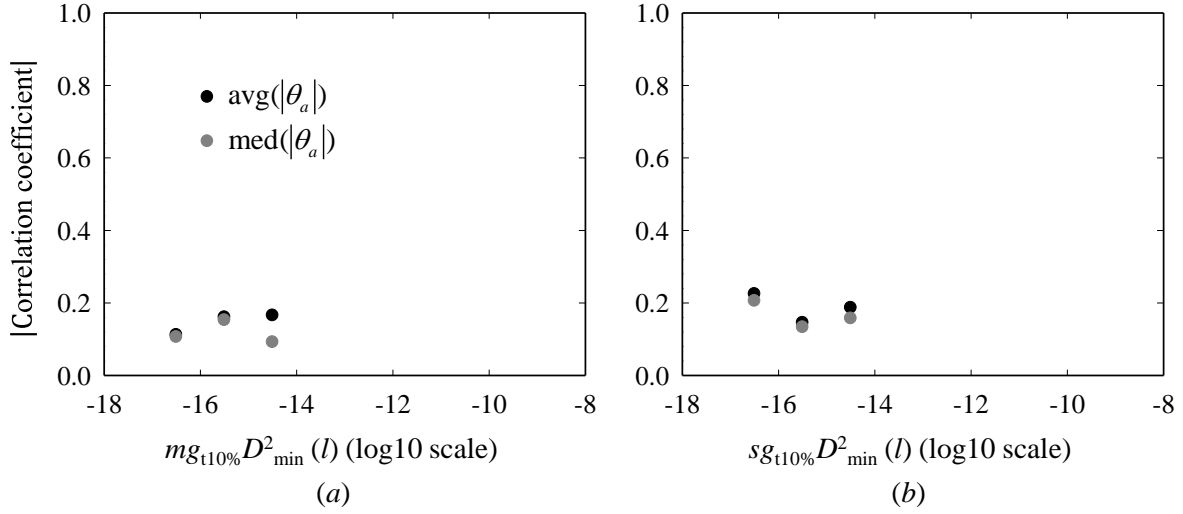


Fig. 8. Graphs of the absolute values of the Spearman correlation coefficients of $\Delta\tau_p$ with both the average and median of the absolute contact angles in GR region across various ranges of (a) $mg_{t10\%}D_{\min}^2$ and (b) $sg_{t10\%}D_{\min}^2$ during long phases in the stick-slip regime. Here, these values are calculated at the last timestep when the number of clusters in the GR region is at its minimum within each phase.

3.4. Sliding friction coefficients and larger particle numbers

In the previous subsections, we studied the relationship between microscopic dynamics and the differential force network, and their link to macroscopic stress fluctuations. The main observations from our study are: (i) particle rearrangement originates from the weakening of a single clustered GR region, and (ii) Correlation analysis shows that the magnitude of the greatest non-affine deformation in the GR region is strongly correlated with the macroscale shear stress drop, and that of neighboring particles is moderately correlated.

We confirmed that these trends were also observed in simulations with various sliding friction coefficients ($\mu_s = 0.1, 0.3, 0.5$, and 0.7) and with a larger number of particles ($\sim 5,000$). The detailed DEM results and analyses are provided in the Supplemental Material [34]. In these simulations, local shear transformation exhibited a nonlinear displacement field with either quadrupolar symmetry or a vortex shape, consistent with previous observations in amorphous materials [41]. Additionally, we studied the influence of the number of clusters in the GR region during a slip event on macroscopic stress change. The results indicate that its effect on macroscopic response is negligible.

4. Discussion

We studied the relationship between the microscopic dynamics, the differential force network, and macroscopic stress fluctuations for 2D sheared granular media. Before the stress drops, while no strong trend was observed between the microscopic dynamics and the differential force network, initial signs of spatial concentration and distribution were noted. During a stress drop, a single clustered GR region was established, in which inter-particle forces significantly decreased. This GR region subsequently featured elevated non-affine motion and D^2_{\min} , the magnitude of which correlated strongly with the macroscale stress drop as noted in the next paragraph.

We used correlation analysis to enhance our quantitative understanding of the relation between particle-scale and macroscale behaviors. During slip events, we found a significant correlation between the magnitude of macroscale stress drops and the greatest D^2_{\min} value, which was observed around the GR region. This strong correlation is due to spatial clustering of the microscopic dynamics and the differential force network. The D^2_{\min} values of the particles immediately surrounding the one with the greatest D^2_{\min} showed a correlation with magnitude of the stress drop, suggesting that STZs are regional events. It should be noted that these STZs do not arise from multiple separate local STZs propagating and connecting but rather propagate from a single STZ that has the greatest D^2_{\min} value. Thus, in an EPM, the non-affine deformation of an STZ should be considered as a regional plastic event rather than a point-like event. This finding supports previous work, including that of Zhang *et al.* [9], which demonstrated correlations between softness and rearrangements but did not explicitly define plastic events as regional. Defining STZs as regional events may not only enhance the predictive accuracy of EPMs but also provide a more comprehensive link to the underlying mechanics.

Finally, we found that local shear transformations exhibited a nonlinear displacement field with either quadrupolar symmetry or a vortex shape. This characteristic of the shear transformation zone should be accounted for in the elastic propagator of an EPM. This comprehensive analysis underscores the interplay between the microscopic dynamics, the differential force network, and the macroscale stress responses, highlighting the critical need to integrate these mechanisms into an EPM for granular materials.

5. Conclusions

We examined the relationship between the microscopic dynamics, the differential force network, and stress fluctuations in 2D sheared granular media. During slip events, particle rearrangement originated from the weakening of a single clustered GR region. The GR region features inter-particle forces experiencing the greatest decrease in magnitude in a given time interval. Using correlation analysis, we found that the

magnitude of the greatest non-affine motion near the single clustered GR region is highly correlated with the macroscale shear stress drop. Moreover, non-affine motion of neighboring particles is also moderately correlated with the shear stress drop. These trends persist in simulations with various sliding friction coefficients and a larger number of particles. On the other hand, the quantity and configuration of clusters in the GR region have minimal impact on macroscale stress drops. Our results indicates that a plastic event is a regional event, not a single-point event and suggest that incorporating regional plastic events into elasto-plastic models can enhance their fidelity to the underlying granular physics. We expect that our findings will contribute to a deeper understanding of plastic deformation in sheared granular media and provide an improved framework for extending elasto-plastic models.

Acknowledgements

This research was supported by the U.S. National Science Foundation CAREER Grant No. CBET-1942096. The authors also gratefully acknowledge partial support from the U.S. Geological Survey Earthquake Hazards Program through Award No. G23AP00268.

Appendix A. Contact Models

The normal contact force, F_n , consists of the normal elastic repulsive force, F_n^e , and the normal damping force, F_n^d , as

$$F_n = F_n^e + F_n^d = k_n \delta_n + \gamma_n \dot{\delta}_n \quad (\text{A1})$$

where k_n is the normal contact stiffness, δ_n is the normal overlapped displacement, γ_n is the viscoelastic damping constant for the normal contact force, and $\dot{\delta}_n$ is the normal relative velocity between the two particles. The k_n for cylindrical bodies can be calculated as [36]

$$k_n = \pi E^* \left[\log(4R_1 / a) + \log(4R_2 / a) - 1 \right]^{-1} \quad (\text{A2})$$

$$\frac{1}{E^*} = \frac{1 - \nu_1^2}{E_1} + \frac{1 - \nu_2^2}{E_2} \quad (\text{A3})$$

where R_1 and R_2 are the radius of particles 1 and 2, respectively, a is the radius of contact area, E_1 and E_2 are Young's modulus of particles 1 and 2, respectively, and ν_1 and ν_2 are Poisson's ratio of particles 1 and 2, respectively. By using the linear damping model [38], the γ_n can be calculated as

$$\gamma_n = 2\alpha\sqrt{k_n m^*} \quad (\text{A4})$$

$$\frac{1}{m^*} = \frac{1}{m_1} + \frac{1}{m_2} \quad (\text{A5})$$

where α is the damping ratio without dimension, and m_1 and m_2 are the mass of particles 1 and 2, respectively.

The tangential contact force, F_t , consists of the tangential elastic repulsive force, F_t^e , and the tangential damping force, F_t^d , as

$$F_t = F_t^e + F_t^d \quad (\text{A6})$$

To consider the effects of various normal contact forces, F_t^e is incrementally calculated as [37, 44]

$$F_t^e = F_t^0 + k_t \Delta \delta_t \quad (\text{A7})$$

where F_t^0 is the tangential contact force at the previous time step, k_t is the tangential contact stiffness, δ_t is the tangential overlapped displacement, and $\Delta \delta_t$ is the incremental tangential overlapped displacement. By using Lai *et al.*'s semi-analytical Hertzian frictional contact model in two dimensions [37], k_t can be calculated as

$$k_t = \pi E^* \left[\log(2R_1 / a) + \log(2R_2 / a) + 1 + w_1^{(a)} \left(\log(4R_1 / a) + \nu_1 / 2(1 - \nu_1) \right) + w_2^{(a)} \left(\log(4R_2 / a) + \nu_2 / 2(1 - \nu_2) \right) \right]^{-1} \quad (\text{A8})$$

Here, $w_1^{(a)}$ and $w_2^{(a)}$ are the penalty factors, which can be calculated as

$$\begin{aligned} w_1^{(a)} &= 0.22 + 2.89(a / R_1) + 0.18\nu_1 - 10.31(a / R_1)^2 + 1.75(a / R_1)\nu_1 + 0.36\nu_1^2 \\ w_2^{(a)} &= 0.22 + 2.89(a / R_2) + 0.18\nu_2 - 10.31(a / R_2)^2 + 1.75(a / R_2)\nu_2 + 0.36\nu_2^2 \end{aligned} \quad (\text{A9})$$

The tangential elastic repulsive force, F_t^e , calculated in Eq. (A7) is subjected to Coulomb's law of friction as

$$F_t^e = \min(F_t^0 + k_t \Delta \delta_t, \mu_s F_n) \quad (\text{A10})$$

where μ_s is the sliding friction coefficient.

The tangential damping force, F_t^d , is calculated as

$$F_t^d = \gamma_t \dot{\delta}_t \quad (\text{A11})$$

where γ_t is the viscoelastic damping constant for tangential force and $\dot{\delta}_t$ is the tangential relative velocity between the two particles. By using the linear damping model [38], the γ_t can be calculated as

$$\gamma_t = 2\alpha\sqrt{k_t m^*} \quad (\text{A12})$$

In the type C elasto-plastic spring-dashpot models [39], the total rolling resistance torque, M_r , consists of a spring torque, M_r^k , and a viscous damping torque, M_r^d , as

$$M_r = M_r^k + M_r^d \quad (\text{A13})$$

This model can be implemented in a computer program in an incremental manner. The incremental spring torque, ΔM_r^k , is calculated from the incremental relative rotation between two particles, $\Delta\theta_r$, and the rolling stiffness, k_r , as

$$\Delta M_r^k = -k_r \Delta\theta_r \quad (\text{A14})$$

where k_r is calculated as [45]

$$k_r = \frac{\pi E^* R_r^2}{4} \quad (\text{A15})$$

$$\frac{1}{R_r} = \frac{1}{R_1} + \frac{1}{R_2} \quad (\text{A16})$$

If the spring torque at time t is $M_{r,t}^k$, the spring torque at time $t + \Delta t$ is given as

$$\begin{cases} M_{r,t+\Delta t}^k = M_{r,t}^k + \Delta M_r^k \\ |M_{r,t+\Delta t}^k| \leq M_r^m \end{cases} \quad (\text{A17})$$

where M_r^m is the limiting spring torque calculated as

$$M_r^m = \mu_r R_r F_n \quad (\text{A18})$$

Here, μ_r is the rolling friction coefficient.

The viscous damping torque M_r^d is assumed to be dependent on the relative rolling angular velocity, $\Delta \dot{\theta}_r$, between the two particles in contact and the rolling viscous damping constant, C_r , such that

$$M_{r,t+\Delta t}^d = \begin{cases} -C_r \dot{\theta}_r & \text{if } |M_{r,t+\Delta t}^d| < M_r^m \\ 0 & \text{if } |M_{r,t+\Delta t}^d| = M_r^m \end{cases} \quad (\text{A19})$$

The C_r is expressed as

$$C_r = \eta_r C_r^{\text{crit}} \quad (\text{A20})$$

where η_r is the rolling viscous damping ratio and C_r^{crit} is the rolling critical viscous damping constant calculated as

$$C_r^{\text{crit}} = 2\sqrt{I_r k_r} \quad (\text{A21})$$

in which I_r is the equivalent moment of inertia for the relative rotational vibration mode about the contact point between the two contacting disks expressed as

$$\frac{1}{I_r} = \frac{1}{I_1 + m_1 R_1^2} + \frac{1}{I_2 + m_2 R_2^2} \quad (\text{A22})$$

where I_1 and I_2 are the moments of inertia of particles 1 and 2, respectively, with respect to their own centroids.

In DEM simulation, to prevent an artificial jump in the elastic tangential overlapped displacement vector, δ_t , δ_t is updated as [46]

$$\delta_t(t_i) = \begin{cases} \delta_t(t_{i-1}) + \mathbf{v}_{c,t}(t_i)(t_i - t_{i-1}) & \text{when } \mathbf{F}_t(t_i) \leq \mu \|\mathbf{F}_n(t_i)\| \\ \delta_t(t_{i-1}) - \frac{1}{k_t(t_i)}(\mathbf{t} \mu_s \|\mathbf{F}_n(t_i)\| - \mu \mathbf{F}_t(t_{i-1})) & \text{when } \mathbf{F}_t(t_i) > \mu \|\mathbf{F}_n(t_i)\| \end{cases} \quad (\text{A23})$$

where t_i and t_{i-1} are the time steps at i and $i-1$, respectively, $\mathbf{v}_{c,t}$ is the tangential component of the relative velocity vector at the contact point of the particles, \mathbf{t} is the unit vector of the tangential interaction, \mathbf{F}_n is the normal contact force vector, and \mathbf{F}_t is the tangential contact force vector.

Appendix B. D_{\min}^2 Computation

As described in the main text, D_{\min}^2 is a measure of the magnitude of the local non-affine deformation.

Specifically, D_{\min}^2 quantifies the mean-square difference between the actual displacements of neighboring particles in the local averaging region relative to a central particle and the displacements that would occur if they were in a uniformly deformed region described by a local affine tensor, Γ . The local averaging regions are defined as regions of radius $r = Nr_p$, where N is an integer, centered on the center of mass of a particle with average radius r_p . Therefore, with a given strain increment at the scale of the system, $\Delta\gamma$, the D_{\min}^2 for a specific particle i can be calculated as [32]

$$D_{\min}^2(\gamma, \Delta\gamma) = \frac{1}{N_i} \sum_j^{N_i} \left\{ \mathbf{r}_j(\gamma) - \mathbf{r}_i(\gamma) - \Gamma [\mathbf{r}_j(\gamma - \Delta\gamma) - \mathbf{r}_i(\gamma - \Delta\gamma)] \right\}^2 \quad (\text{B1})$$

where γ is the macroscopic shear strain of a given time, N_i is the number of the neighbor particles of the particle i within a local average region, and j represents the neighboring particles of the particle i . At a given strain, $\gamma - \Delta\gamma$, particles j that surround the particle i are defined to form its neighborhood. $\mathbf{r}_i(\gamma)$ and $\mathbf{r}_j(\gamma)$ are the vectors from the origin of coordinate systems to the location of the particles i and j at a given strain, γ , respectively. The locally best-fit affine tensor, Γ , can be obtained by minimizing the quantity D_{\min}^2 as [4]

$$\mathbf{X} = \sum_j^{N_i} [\mathbf{r}_j(\gamma) - \mathbf{r}_i(\gamma)] \otimes [\mathbf{r}_j(\gamma - \Delta\gamma) - \mathbf{r}_i(\gamma - \Delta\gamma)] \quad (\text{B2})$$

$$\mathbf{Y} = \sum_j^{N_i} [\mathbf{r}_j(\gamma - \Delta\gamma) - \mathbf{r}_i(\gamma - \Delta\gamma)] \otimes [\mathbf{r}_j(\gamma - \Delta\gamma) - \mathbf{r}_i(\gamma - \Delta\gamma)] \quad (\text{B3})$$

$$\Gamma = \mathbf{X} \cdot \mathbf{Y}^{-1} \quad (\text{B4})$$

References

- [1] Spaepen, F. (1977). A microscopic mechanism for steady state inhomogeneous flow in metallic glasses. *Acta Metallurgica*, 25(4), 407-415.
- [2] Argon, A. S. (1979). Plastic deformation in metallic glasses. *Acta metallurgica*, 27(1), 47-58.
- [3] Steif, P. S., Spaepen, F., & Hutchinson, J. W. (1982). Strain localization in amorphous metals. *Acta Metallurgica*, 30(2), 447-455.
- [4] Falk, M. L., & Langer, J. S. (1998). Dynamics of viscoplastic deformation in amorphous solids. *Physical Review E*, 57(6), 7192.
- [5] Langer, J. S. (2001). Microstructural shear localization in plastic deformation of amorphous solids. *Physical Review E*, 64(1), 011504.
- [6] Picard, G., Ajdari, A., Lequeux, F., & Bocquet, L. (2004). Elastic consequences of a single plastic event: A step towards the microscopic modeling of the flow of yield stress fluids. *The European Physical*

Journal E, 15, 371-381.

- [7] Picard, G., Ajdari, A., Lequeux, F., & Bocquet, L. (2005). Slow flows of yield stress fluids: Complex spatiotemporal behavior within a simple elastoplastic model. *Physical Review E*, 71(1), 010501.
- [8] Nicolas, A., Ferrero, E. E., Martens, K., & Barrat, J. L. (2018). Deformation and flow of amorphous solids: Insights from elastoplastic models. *Reviews of Modern Physics*, 90(4), 045006.
- [9] Zhang, G., Ridout, S. A., & Liu, A. J. (2021). Interplay of rearrangements, strain, and local structure during avalanche propagation. *Physical Review X*, 11(4), 041019.
- [10] Cubuk, E. D., Schoenholz, S. S., Rieser, J. M., Malone, B. D., Rottler, J., Durian, D. J., ... & Liu, A. J. (2015). Identifying structural flow defects in disordered solids using machine-learning methods. *Physical Review Letters*, 114(10), 108001.
- [11] Patinet, S., Vandembroucq, D., & Falk, M. L. (2016). Connecting local yield stresses with plastic activity in amorphous solids. *Physical Review Letters*, 117(4), 045501.
- [12] Cubuk, E. D., Ivancic, R. J. S., Schoenholz, S. S., Strickland, D. J., Basu, A., Davidson, Z. S., ... & Liu, A. J. (2017). Structure-property relationships from universal signatures of plasticity in disordered solids. *Science*, 358(6366), 1033-1037.
- [13] Barbot, A., Lerbinger, M., Hernandez-Garcia, A., García-García, R., Falk, M. L., Vandembroucq, D., & Patinet, S. (2018). Local yield stress statistics in model amorphous solids. *Physical Review E*, 97(3), 033001.
- [14] Richard, D., Ozawa, M., Patinet, S., Stanifer, E., Shang, B., Ridout, S. A., ... & Manning, M. L. (2020). Predicting plasticity in disordered solids from structural indicators. *Physical Review Materials*, 4(11), 113609.
- [15] Xu, B., Falk, M. L., Patinet, S., & Guan, P. (2021). Atomic nonaffinity as a predictor of plasticity in amorphous solids. *Physical Review Materials*, 5(2), 025603.
- [16] Ruan, D., Patinet, S., & Falk, M. L. (2022). Predicting plastic events and quantifying the local yield surface in 3D model glasses. *Journal of the Mechanics and Physics of Solids*, 158, 104671.
- [17] Stanifer, E., & Manning, M. L. (2022). Avalanche dynamics in sheared athermal particle packings occurs via localized bursts predicted by unstable linear response. *Soft Matter*, 18(12), 2394-2406.
- [18] Zhai, C., Albayrak, N., Engqvist, J., Hall, S. A., Wright, J., Majkut, M., ... & Hurley, R. C. (2022). Quantifying local rearrangements in three-dimensional granular materials: Rearrangement measures, correlations, and relationship to stresses. *Physical Review E*, 105(1), 014904.
- [19] Cates, M. E., Wittmer, J. P., Bouchaud, J. P., & Claudin, P. (1998). Jamming, force chains, and fragile matter. *Physical Review Letters*, 81(9), 1841.
- [20] Radjai, F., Wolf, D. E., Jean, M., & Moreau, J. J. (1998). Bimodal character of stress transmission in

- granular packings. *Physical Review Letters*, 80(1), 61.
- [21] Peters, J. F., Muthuswamy, M., Wibowo, J., & Tordesillas, A. (2005). Characterization of force chains in granular material. *Physical Review E*, 72(4), 041307.
- [22] Tordesillas, A. (2007). Force chain buckling, unjamming transitions and shear banding in dense granular assemblies. *Philosophical Magazine*, 87(32), 4987-5016.
- [23] Tordesillas, A., & Muthuswamy, M. (2008). A thermomicromechanical approach to multiscale continuum modeling of dense granular materials. *Acta Geotechnica*, 3, 225-240.
- [24] Tordesillas, A., & Muthuswamy, M. (2009). On the modeling of confined buckling of force chains. *Journal of the Mechanics and Physics of Solids*, 57(4), 706-727.
- [25] Tordesillas, A., Lin, Q., Zhang, J., Behringer, R. P., & Shi, J. (2011). Structural stability and jamming of self-organized cluster conformations in dense granular materials. *Journal of the Mechanics and Physics of Solids*, 59(2), 265-296.
- [26] Kramár, M., Cheng, C., Basak, R., & Kondic, L. (2022). On intermittency in sheared granular systems. *Soft Matter*, 18(18), 3583-3593.
- [27] Bretz, P., Kondic, L., & Kramar, M. (2023). Stochastic methods for slip prediction in a sheared granular system. *Physical Review E*, 107(5), 054901.
- [28] Gupta, A., Ramesh, K. T., & Hurley, R. C. (2024). Instabilities in a two-dimensional granular fault gouge: Particle dynamics and stress fluctuations. *Journal of the Mechanics and Physics of Solids*, 105843.
- [29] Ma, G., Zou, Y., Chen, Y., Tang, L., Ng, T. T., & Zhou, W. (2021). Spatial correlation and temporal evolution of plastic heterogeneity in sheared granular materials. *Powder Technology*, 378, 263-273.
- [30] Ma, G., Mei, J., Gao, K., Zhao, J., Zhou, W., & Wang, D. (2022). Machine learning bridges microslips and slip avalanches of sheared granular gouges. *Earth and Planetary Science Letters*, 579, 117366.
- [31] Mei, J., Ma, G., Wang, Q., Wu, T., & Zhou, W. (2022). Micro-and macroscopic aspects of the intermittent behaviors of granular materials related by graph neural network. *International Journal of Solids and Structures*, 251, 111763.
- [32] Mei, J., Ma, G., Tang, L., Gao, K., Cao, W., & Zhou, W. (2023). Spatial clustering of microscopic dynamics governs the slip avalanche of sheared granular materials. *International Journal of Plasticity*, 163, 103570.
- [33] Kloss, C., Goniva, C., Hager, A., Amberger, S., & Pirker, S. (2012). Models, algorithms and validation for opensource DEM and CFD-DEM. *Progress in Computational Fluid Dynamics, an International Journal*, 12(2-3), 140-152.
- [34] See Supplemental Material at [URL will be inserted by publisher] for the DEM results of simulations with various sliding friction coefficients and a larger number of particles.

- [35] Da Cruz, F., Emam, S., Prochnow, M., Roux, J. N., & Chevoir, F. (2005). Rheophysics of dense granular materials: Discrete simulation of plane shear flows. *Physical Review E*, 72(2), 021309.
- [36] Johnson, K. L. (1985). *Contact mechanics*. Cambridge university press.
- [37] Lai, Z., Chen, Q., & Huang, L. (2021). A semianalytical Hertzian frictional contact model in 2D. *Applied Mathematical Modelling*, 92, 546-564.
- [38] Hu, G., Hu, Z., Jian, B., Liu, L., & Wan, H. (2010, August). On the determination of the damping coefficient of non-linear spring-dashpot system to model hertz contact for simulation by discrete element method. In *2010 WASE International Conference on Information Engineering* (Vol. 3, pp. 295-298). IEEE.
- [39] Ai, J., Chen, J. F., Rotter, J. M., & Ooi, J. Y. (2011). Assessment of rolling resistance models in discrete element simulations. *Powder Technology*, 206(3), 269-282.
- [40] Hieronymus-Schmidt, V., Rösner, H., Wilde, G., & Zacccone, A. (2017). Shear banding in metallic glasses described by alignments of Eshelby quadrupoles. *Physical Review B*, 95(13), 134111.
- [41] Shi, R. H., Wu, Y. C., Shuang, F., & Zhang, Z. W. (2023). Dipolar and quadrupolar characteristics of shear transformation in two dimensional metallic glasses. *Materials Today Communications*, 34, 105389.
- [42] The MathWorks, Inc. (2020). *MATLAB* (Version 9.8 R2020a) [Software]. Natick, MA: The MathWorks, Inc.
- [43] Meloun, M., & Militky, J. (2011). *Statistical data analysis: A practical guide*. Woodhead Publishing, Limited.
- [44] Di Renzo, A., & Di Maio, F. P. (2005). An improved integral non-linear model for the contact of particles in distinct element simulations. *Chemical Engineering Science*, 60(5), 1303-1312.
- [45] Bardet, J. P., & Huang, Q. (1993). Rotational stiffness of cylindrical particle contacts. *Proceedings of the 2 nd International Conference on Micromechanics of Granular Media*. Birmingham, UK, C. Thornton, ed., 39-44.
- [46] Zabulionis, D., Kacianauskas, R., Markauskas, D., & Rojek, J. (2012). An investigation of nonlinear tangential contact behaviour of a spherical particle under varying loading. *Bulletin of the Polish Academy of Sciences. Technical Sciences*, 60(2), 265-278.

Supplemental Material: The Interplay Between Forces, Particle Rearrangements, and Macroscopic Stress Fluctuations in Sheared 2D Granular Media

Kwangmin Lee ^a, Ryan C. Hurley ^{a, b *}

^a *Department of Mechanical Engineering, Johns Hopkins University, Baltimore, Maryland 21218, USA*

^b *Hopkins Extreme Materials Institute, Johns Hopkins University, Baltimore, Maryland 21218, USA*

S1. Sliding Friction Coefficients

To study the effect of sliding friction coefficients on stick-slip behavior, we conducted additional DEM simulations with μ_s values including 0.1, 0.3, and 0.5, to complement the simulation with a μ_s value of 0.7 described in Sections 2 and 3. The boundary conditions, material properties, and contact properties otherwise remained the same as those used in the DEM simulation described in Section 2.

Figure S1 displays the normalized shear stress-strain curves for various sliding friction coefficients. In the stick-slip regime (shear strain ≥ 2.2 %), curves for $\mu_s = 0.1, 0.3, 0.5$, and 0.7 were similar. During the slip events, the microscopic dynamics and the differential force network for $\mu_s = 0.1, 0.3$, and 0.5 followed a similar trend to those observed for $\mu_s = 0.7$, which are explained in Section 3.2.

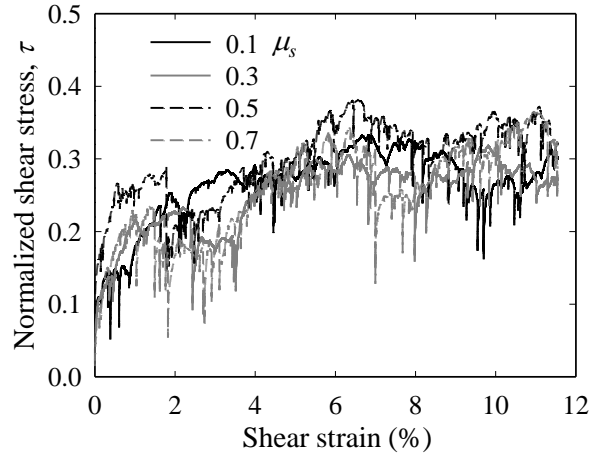


Fig. S1. Normalized shear stress-strain curve from discrete element method simulation for various sliding friction coefficients.

Employing a dataset that includes approximately 130,000 timesteps for each of four simulations with

sliding friction coefficients ($\mu_s = 0.1, 0.3, 0.5$, and 0.7), we observed approximately 18,000 phases for $\mu_s = 0.1$, 46,000 for $\mu_s = 0.3$, 52,000 for $\mu_s = 0.5$, and 42,000 for $\mu_s = 0.7$ within the stick-slip regime. We examined the correlations between various parameters and $\Delta\tau$ across these timesteps or $\Delta\tau_p$ across these phases. Figure S2 illustrates the absolute values of the Spearman correlation coefficients between kinematic measures and $\Delta\tau$ or $\Delta\tau_p$ for various sliding friction coefficients, with each value of μ_s represented by different symbols, in the stick-slip regime. Specifically: (a) shows the correlation coefficient between $\Delta\tau$ and $g_{t10\%}D_{\min}^2$ across all instantaneous timesteps, (b) depicts the correlation coefficient between $\Delta\tau_p$ and $mg_{t10\%}D_{\min}^2$ for all phases, (c) displays the correlation coefficient between $\Delta\tau_p$ and $mg_{t10\%}D_{\min}^2$ for long (l) phases, where t_p is greater than $3\Delta\gamma$, (d) shows the correlation coefficient between $\Delta\tau_p$ and $mg_{t10\%}D_{\min}^2$ for short (s) phases, where t_p is less than or equal to $3\Delta\gamma$, (e) displays the partial correlation coefficient between $\Delta\tau_p$ and $mg_{t10\%}D_{\min}^2$ excluding the effect of gD_{\min}^2 for long phases, (f) displays the correlation coefficient between $\Delta\tau_p$ and mgD_{\min}^2 for long phases, (g) depicts the correlation coefficient between $\Delta\tau_p$ and $sg_{t10\%}D_{\min}^2$ for all phases, (h) displays the correlation coefficient between $\Delta\tau_p$ and $sg_{t10\%}D_{\min}^2$ for long phases, (i) shows the correlation coefficient between $\Delta\tau_p$ and $sg_{t10\%}D_{\min}^2$ for short phases, (j) displays the correlation coefficient between $\Delta\tau_p$ and sgD_{\min}^2 for long phases, and (k) shows the correlation coefficient between $\Delta\tau_p$ and t_p for long phases.

Figure S2a-j demonstrates consistent trends in the correlations between $\Delta\tau$ and $g_{t10\%}D_{\min}^2$ across all instantaneous timesteps and between $\Delta\tau_p$ and both $mg_{t10\%}D_{\min}^2$ and $sg_{t10\%}D_{\min}^2$ for all phases, long phases, and short phases, for all μ_s values. Figure S2a-b and g shows that the correlations between $\Delta\tau_p$ and both $mg_{t10\%}D_{\min}^2$ and $sg_{t10\%}D_{\min}^2$ across all phases during the slip events ($\Delta\tau_p < 0$) mostly have stronger associations compared to those of $\Delta\tau$ with $g_{t10\%}D_{\min}^2$ across all instantaneous timesteps during the slip events ($\Delta\tau < 0$) for all μ_s values. These stronger correlations observed for all phases, as opposed to individual timesteps, indicate that examining the microscopic dynamics over the entire duration of a phase provides a better understanding of the macroscale responses of granular materials. Figure S2b-c and g-h shows that $\Delta\tau_p - mg_{t10\%}D_{\min}^2$ and $\Delta\tau_p - sg_{t10\%}D_{\min}^2$ in long phases not only follow the same trend as those observed in all phases but are also more highly correlated, particularly during the slip events ($\Delta\tau_p < 0$) across all μ_s values. The correlations between $\Delta\tau_p$ and both $mg_{t10\%}D_{\min}^2$ and $sg_{t10\%}D_{\min}^2$ for long phases are strong for a significant decrease in $\Delta\tau_p$ ($\Delta\tau_p < -10^{-2}$) and mostly moderate for a small decrease in $\Delta\tau_p$ ($10^{-2} < \Delta\tau_p < 0$) across all μ_s values. On the other hand, Figure S2d and i shows that $\Delta\tau_p - mg_{t10\%}D_{\min}^2$ and $\Delta\tau_p - sg_{t10\%}D_{\min}^2$ in short phases are not strongly correlated for all $\Delta\tau_p$ regimes across all μ_s values. This is because τ can show fluctuations during short phases, as depicted in Stage III shown in Figure 2b, when the structure is

unstable. Figure S2*c,f, h, and j* shows that the correlations between $\Delta\tau_p$ and both $mg_{t10\%}D_{\min}^2$ and $sg_{t10\%}D_{\min}^2$ for long phases are consistently stronger than those between $\Delta\tau_p$ and both mgD_{\min}^2 and sgD_{\min}^2 for long phases during the slip events ($\Delta\tau_p < 0$), indicating that variability in D_{\min}^2 values of particles surrounding the one with the greatest D_{\min}^2 value influences $\Delta\tau_p$ to some extent during the slip events for all μ_s values. Figure S2*e* indicates that the partial correlations between $\Delta\tau_p$ and $mg_{t10\%}D_{\min}^2$ excluding the effect of gD_{\min}^2 for long phases are mostly moderate for larger events ($\Delta\tau_p < -10^{-2}$), supporting our earlier argument that these long slip events are regional rather than point-like phenomena. Figure S2*c and h* shows that during the slip events ($\Delta\tau_p < 0$), the correlations between $\Delta\tau_p$ and $sg_{t10\%}D_{\min}^2$ are almost equal to or stronger than those between $\Delta\tau_p$ and $mg_{t10\%}D_{\min}^2$ in long phases for different μ_s values. This suggests that the phenomenon is dependent on its history for all μ_s values, as $sg_{t10\%}D_{\min}^2$ captures the overall behavior of particle rearrangements throughout a slip event. Figure S2*k* illustrates varying trends in the correlation between $\Delta\tau_p$ and t_p for long phases for different μ_s values. Notably, in certain stick phases where $\Delta\tau_p$ significantly increases ($10^{-3} < \Delta\tau_p < 10^{-1}$), moderate correlations between $\Delta\tau_p$ and t_p are observed at $\mu_s = 0.5$ and 0.7 . In contrast, at lower μ_s values (0.1 and 0.3), these correlations are weak or have high P -values (> 0.05), possibly due to increased particle movement during stick phases at lower sliding friction levels.

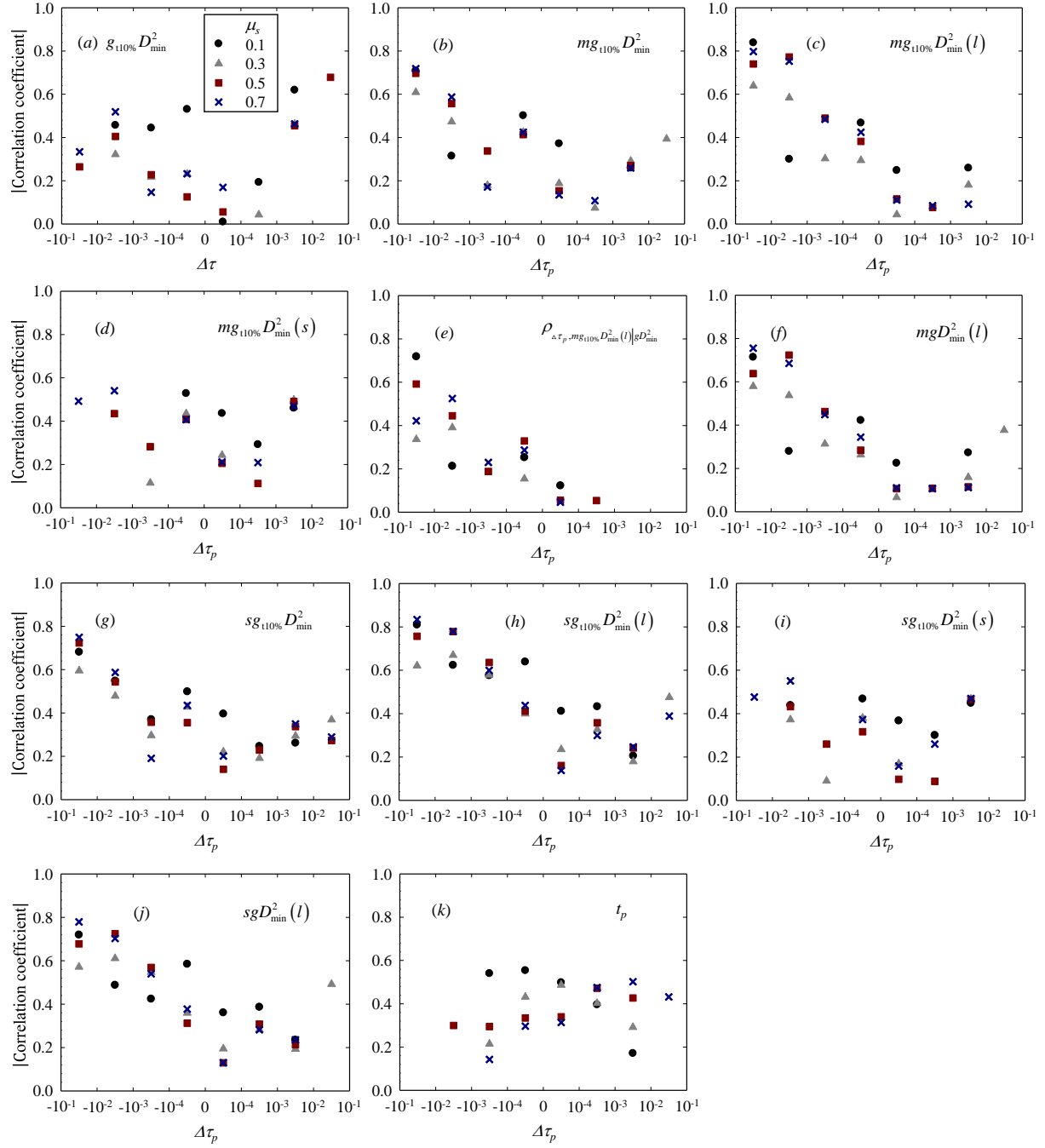


Fig. S2. Graphs of the absolute values of the Spearman correlation coefficients between kinematic measures and $\Delta\tau$ or $\Delta\tau_p$ for various sliding friction coefficients, with each value of μ_s represented by different symbols, in the stick-slip regime; (a) $\Delta\tau - g_{t10\%}D_{\min}^2$ across all instantaneous timesteps, (b) $\Delta\tau_p - mg_{t10\%}D_{\min}^2$ for all phases, (c) $\Delta\tau_p - mg_{t10\%}D_{\min}^2$ for long, l , ($> 3\lambda$) phases, (d) $\Delta\tau_p - mg_{t10\%}D_{\min}^2$ for short, s , ($\leq 3\lambda$) phases, (e) $\Delta\tau_p - mg_{t10\%}D_{\min}^2$ for long phases (partial correlation excluding the effect of gD_{\min}^2), (f) $\Delta\tau_p - mgD_{\min}^2$ for long phases, (g) $\Delta\tau_p - sg_{t10\%}D_{\min}^2$ for all phases, (h) $\Delta\tau_p - sg_{t10\%}D_{\min}^2$ for long phases, (i) $\Delta\tau_p - sg_{t10\%}D_{\min}^2$ for short phases, (j) $\Delta\tau_p - sgD_{\min}^2$ for long phases, and (k) $\Delta\tau_p - t_p$ for long phases.

S2. Larger Particle Numbers

To investigate the effect of the number of particles on the microscopic dynamics, the differential force network, and the statistical response during stick-slip behavior, we conducted additional DEM simulations using a larger number of particles. We selected a uniform distribution of particle sizes ranging from 0.2 to 0.4 μm for the particle radius. The total number of particles used was about 5,000. Except for particle sizes, the boundary conditions, material properties, and contact properties were consistent with those used in the DEM model described in Section 2. In particular, for the sliding friction coefficients, μ_s , and rolling friction coefficients, μ_r , values of 0.7 and 0.01 were used, respectively. The macroscale shear strain interval at which simulation data were output for analysis, $\Delta\gamma$, was 1.8×10^{-6} .

The normalized shear stress-strain curve for both simulations with a small and large number of particles is presented in Figure S3a. This figure shows that the average value of the normalized shear stress in the steady-state regime (shear strain $\geq 5.4\%$) for a large number of particles is similar to the average value of the normalized shear stress at the stick-slip regime (shear strain $\geq 2.2\%$) for a smaller number of particles. In the normalized shear stress-strain curve depicted in Fig. S3a, the steady-state regime is identified as the region where the shear strain exceeds 5.4%. This designation is based on the observation that, beyond this point, the normalized shear stress exhibits a relatively stable and consistent pattern compared to the initial deformation before 5.4% shear strain. The simulation with a larger number of particles exhibits smaller magnitudes of normalized shear stress fluctuations compared to those with a small number of particles. Figure S4 provides the normalized shear stress-strain curves for various sliding friction coefficients in simulations with a larger number of particles.

During the shearing process of the simulation with a larger number of particles, we observed a total of approximately 26,000 phases in the steady-state regime, comprising both stick (ascending) and slip (descending) events in the normalized shear stress-strain curve. Here, we first focused on the region around the largest stress drop observed in the steady-state regime, specifically between 9.380% to 9.384% shear strain as depicted in Fig. S3b. This region around the slip event is delineated into three distinct stages: pre-stress drop (Stage I), stress drop (Stage II), and post-stress drop (Stage III). Here, in Stage II, there were two stress drops. The largest stress drop in the steady-state regime corresponds to the first drop. Right after the first stress drop, we observed one more stress drop (second drop). Figures S5-S8 show the particles experiencing the greatest 1% reduction in inter-particle force magnitude, the differential force network, the particles experiencing the greatest 1% D^2_{\min} , and the full D^2_{\min} field in Stages I-III during 9.380 - 9.384% shear strain. Rattler particles are again excluded from the computation of D^2_{\min} . The colorless disks in the D^2_{\min} field graphs in Figures S5-S8 are the rattler particles.

As observed in the simulation with fewer particles (Section 3.2, see Fig. 3), the simulation with a larger number of particles also exhibited the same trends in the microscopic dynamics and the differential force network around the major stress drop region, except that it has two stress drops in Stage II. In this simulation, the initial random distribution of the differential force and D^2_{\min} (Fig. S5) rapidly consolidated into a single cluster in the lower left part of the sample by Step 4 (Fig. S6), indicating the formation of a single clustered GR region and the beginning of the first stress drop. This clustering process, similar to what was observed in simulations with fewer particles, highlights the reproducibility of such phenomena across samples of different sizes. From Step 5, the single clustered GR region collapsed, with differential force changes spreading from the location where the single clustered GR region had been established (Fig. S6). This continued rearrangement near this clustered region showed a significant structural change, and it influenced the macroscopic stress response. Notably, outside this clustered region, changes in inter-particle forces remained minimal during Steps 4-5 (Fig. S6), pointing to a focused area of activity that led to a significant stress drop in the normalized macroscopic shear stress-strain curve. At Step 10, the distribution of the differential force and D^2_{\min} (Fig. S7) rapidly consolidated into a single cluster again in the lower right part of the sample, indicating the formation of another single clustered GR region and the start of the second stress drop. From Step 11, this GR region collapsed, with differential force changes spreading from its location (Fig. S7). By Stage III, the spread of differential force changes from the collapse of the GR region subsided, and both differential force and D^2_{\min} appeared randomly distributed once more in Stage III (Fig. S8).

Figure S9 displays the non-affine displacement field observed in a simulation with a large number of particles throughout Stages I-III. A distinct region of concentrated non-affine displacement was observed at Steps 5-6 at the beginning of the first stress drop. This region coincided with the single clustered region of high D^2_{\min} at Steps 4-5 in Figure S6. During these steps, the non-affine displacement field exhibited quadrupolar symmetry, consistent with previous observations in amorphous materials [39-40]. Similarly, at Steps 10-11, a distinct STZ was observed. This region coincided with the single clustered region of high D^2_{\min} at Step 10 in Figure S7 at the beginning of the second stress drop. During these steps, the non-affine displacement field exhibited a vortex shape, also consistent with previous observations in amorphous materials [40].

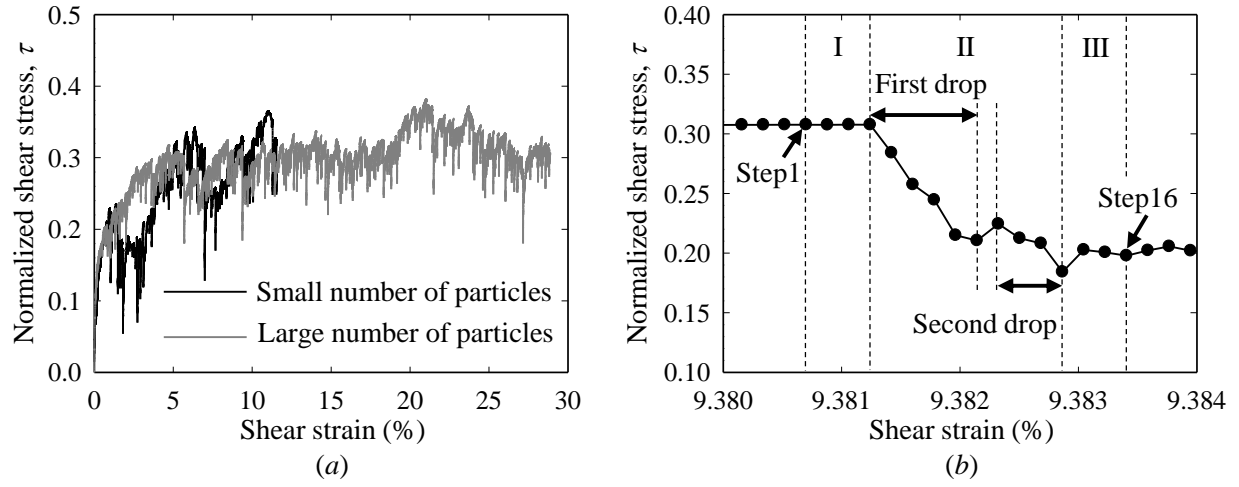


Fig. S3. (a) Normalized shear stress-strain curve from discrete element method simulation for a small and a large number of particles. (b) Normalized shear stress-strain curve around a slip event during 9.380% to 9.384% shear strain for a simulation with a large number of particles; the region around the slip event is delineated into three distinct stages: the pre-stress drop stage (Stage I), the stress drop stage (Stage II), and the post-stress drop stage (Stage III). The first and second stress drops are indicated.

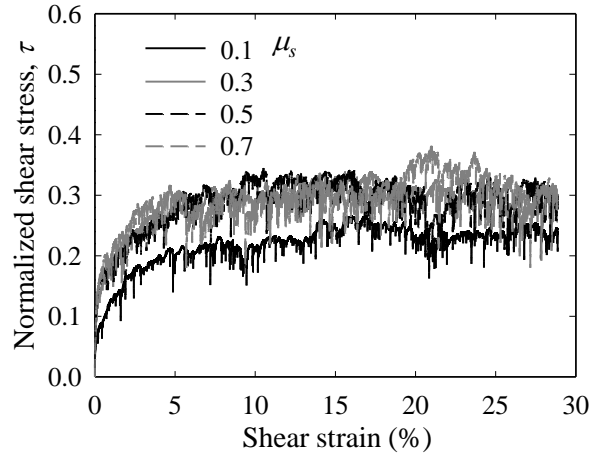


Fig. S4. Normalized shear stress-strain curve from discrete element method simulation with a large number of particles for various sliding friction coefficients.

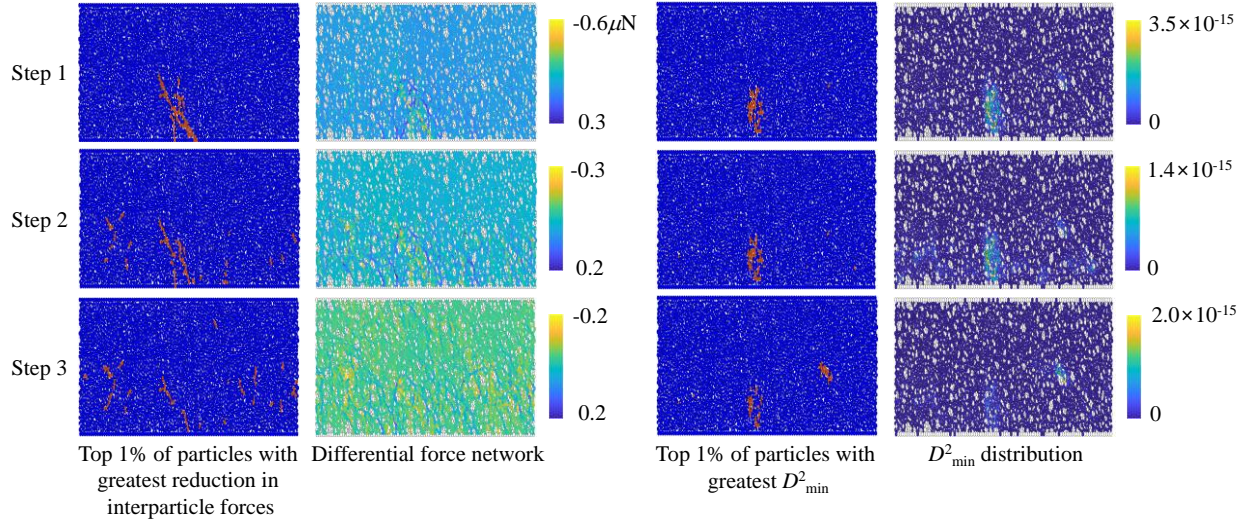


Fig. S5. Top 1% of particles with the greatest reduction in inter-particle forces magnitude, differential force network, top 1% of particles with greatest D^2_{\min} , and the D^2_{\min} field at each $\Delta\gamma$ increment in Stage I for the simulation with a large number of particles.

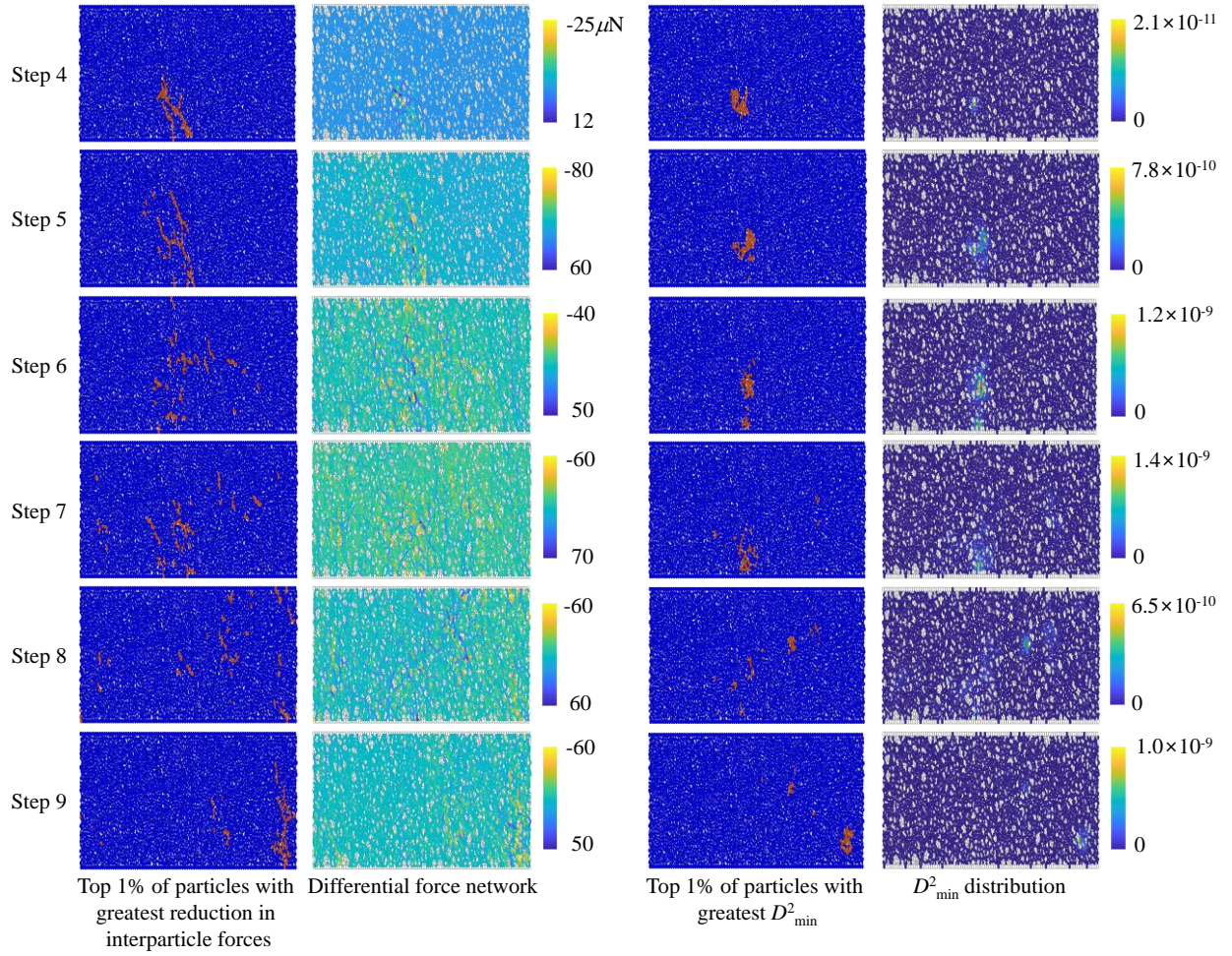


Fig. S6. Top 1% of particles with the greatest reduction in inter-particle forces magnitude, differential force network, top 1% of particles with greatest D^2_{\min} , and the D^2_{\min} field at each $\Delta\gamma$ increment in Stage II during the first stress drop for the simulation with a large number of particles.

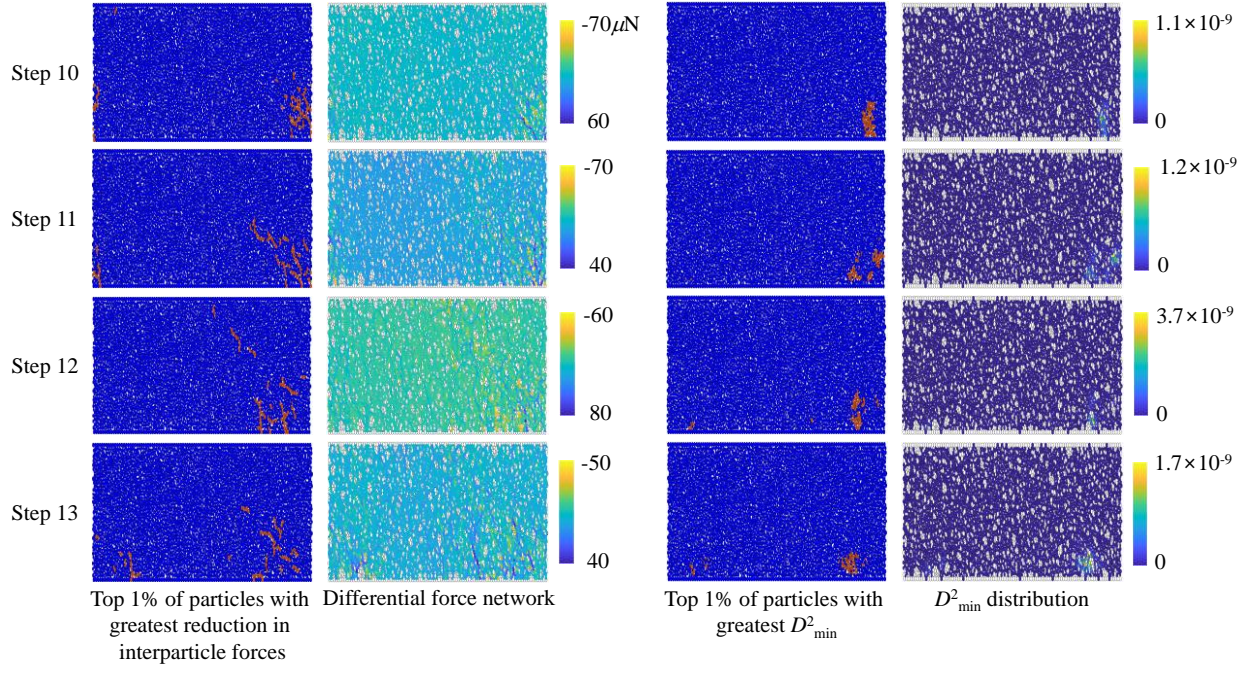


Fig. S7. Top 1% of particles with the greatest reduction in inter-particle forces magnitude, differential force network, top 1% of particles with greatest D^2_{\min} , and the D^2_{\min} field at each $\Delta\gamma$ increment in Stage II during the second stress drop for the simulation with a large number of particles.

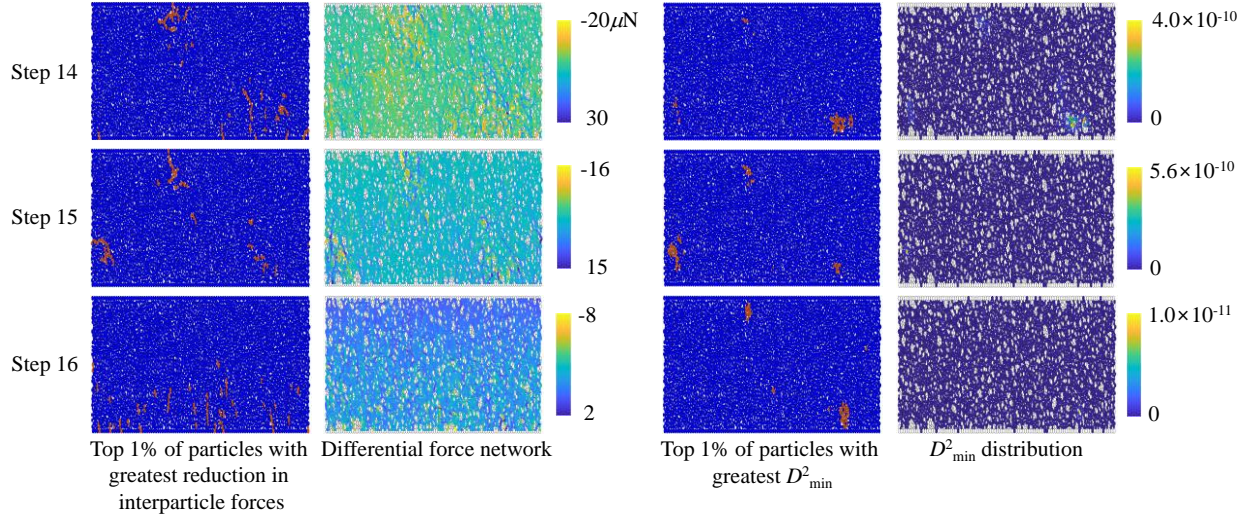


Fig. S8. Top 1% of particles with the greatest reduction in inter-particle forces magnitude, differential force network, top 1% of particles with greatest D^2_{\min} , and the D^2_{\min} field at each $\Delta\gamma$ increment in Stage III for the simulation with a large number of particles.

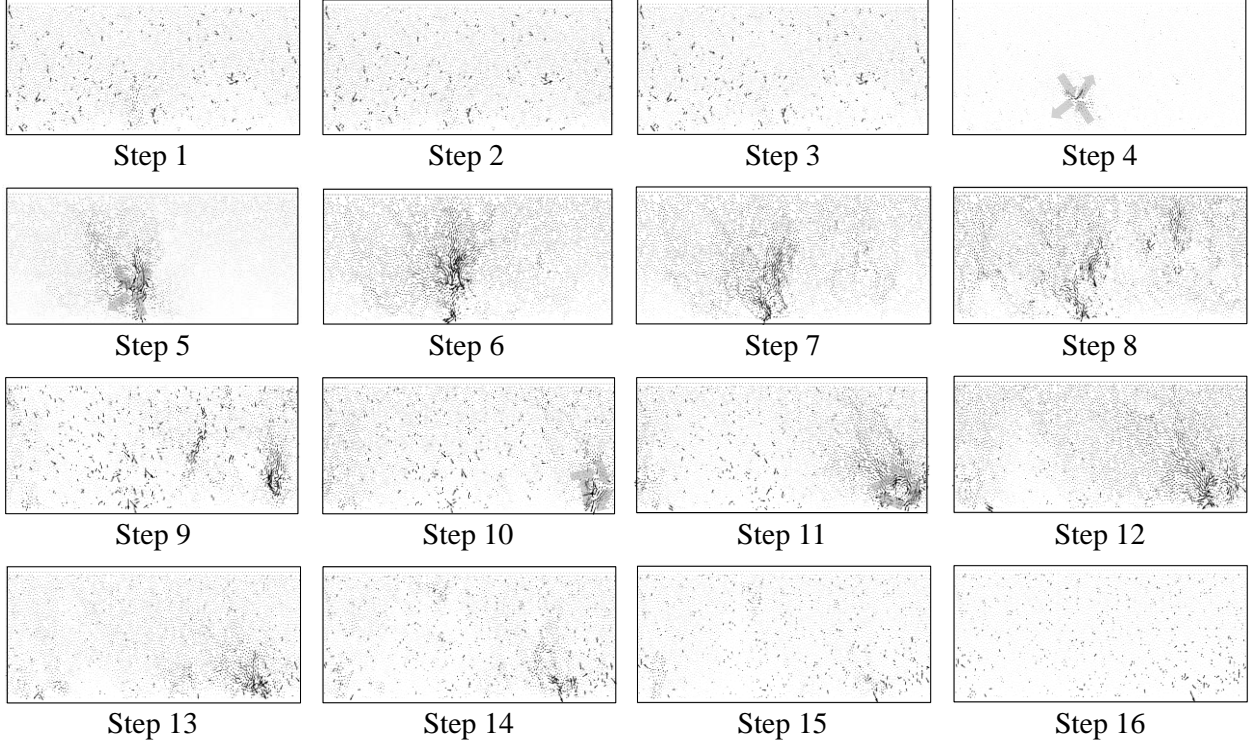


Fig. S9. Non-affine displacement field around the slip event for the simulation with a large number of particles. The arrows represent the non-affine displacement vectors, with the length of each arrow indicating its relative magnitude. Note that the arrow lengths are scaled differently for each step to highlight relative displacements. The gray arrows in Steps 4-5 indicate the directions of tension and compression, and the gray arrows in Steps 10-11 indicate vortex-like flow.

Figure S10 shows (a) the Spearman correlation coefficient between $|\Delta\sigma_p|$ and D_{\min}^2 at particles, (b) the greatest D_{\min}^2 and the average of the greatest top 10% D_{\min}^2 magnitudes, (c) the number of clusters in the GR region, and (d) the average and median of the absolute values of contact angles in the GR region during the 9.380 – 9.384% sample shear strain for the simulation with a large number of particles. These correlations and variables follow the same trends as those from the simulation with a smaller number of particles (Fig. 5). Figures 5a and S10a show that, in both simulations, the Spearman correlation coefficients between $|\Delta\sigma_p|$ and D_{\min}^2 at particles are relatively high at the beginning of the stress drops in Stage II because particle rearrangement was caused by the weakening of the single clustered GR region. Figures 5b and S10b show that both gD_{\min}^2 and $g_{\text{t10\%}}D_{\min}^2$ increased in Stage II and decreased in Stage III in both simulations with a smaller and larger number of particles. We also note that the maximum values of gD_{\min}^2 and $g_{\text{t10\%}}D_{\min}^2$ in both simulations during Stage II were almost the same. Figures 5c and S10c illustrate that the number of clusters in the GR region in both simulations drop dramatically at the beginning of the stress

drops in Stage II. Figures 5*d* and S10*d* show that the average and the median of the absolute values of the contact angles in the GR region fluctuated significantly from Stage II in both simulations.

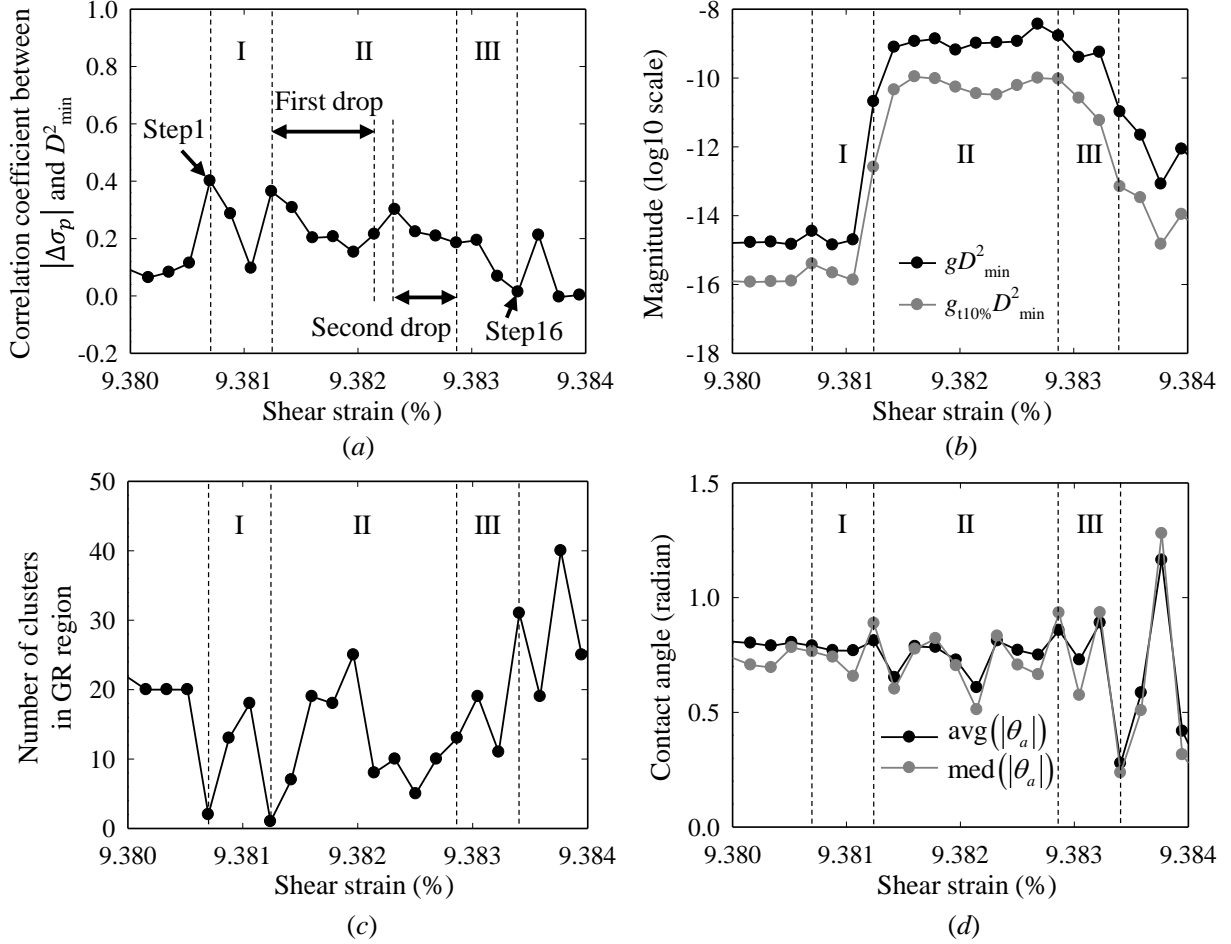


Fig. S10. (a) The Spearman correlation coefficients between the absolute values of maximum principal stress change, $|\Delta\sigma_p|$, and D_{\min}^2 at particles, (b) the greatest D_{\min}^2 and the average of greatest top 10% D_{\min}^2 magnitudes, (c) the number of clusters in the GR region, and (d) the average and the median of the absolute values of the contact angles in the GR region during 9.380 to 9.384% sample shear strain in the simulation with a large number of particles. The first stress drop and the second stress drop are indicated.

Figure S11 illustrates the Spearman correlation coefficients between kinematic measures and $\Delta\tau$ or $\Delta\tau_p$ for simulations with a smaller number of particles in the stick-slip regime and a larger number of particles in the steady-state regime, with each correlation represented by different colors. Specifically: (a) shows the correlation coefficient between $\Delta\tau$ and $g_{t10\%}D_{\min}^2$ across all instantaneous timesteps, (b) depicts the

correlation coefficient between $\Delta\tau_p$ and $mg_{t10\%}D_{\min}^2$ for all phases, (c) displays the correlation coefficient between $\Delta\tau_p$ and $mg_{t10\%}D_{\min}^2$ for long (*l*) phases, where t_p is greater than $3\Delta\gamma$, (d) shows the correlation coefficient between $\Delta\tau_p$ and $mg_{t10\%}D_{\min}^2$ for short (*s*) phases, where t_p is less than or equal to $3\Delta\gamma$, (e) displays the partial correlation coefficient between $\Delta\tau_p$ and $mg_{t10\%}D_{\min}^2$ excluding the effect of gD_{\min}^2 for long phases, (f) displays the correlation coefficient between $\Delta\tau_p$ and mgD_{\min}^2 for long phases, (g) depicts the correlation coefficient between $\Delta\tau_p$ and $sg_{t10\%}D_{\min}^2$ for all phases, (h) displays the correlation coefficient between $\Delta\tau_p$ and $sg_{t10\%}D_{\min}^2$ for long phases, (i) shows the correlation coefficient between $\Delta\tau_p$ and $sg_{t10\%}D_{\min}^2$ for short phases, (j) displays the correlation coefficient between $\Delta\tau_p$ and sgD_{\min}^2 for long phases, and (k) shows the correlation coefficient between $\Delta\tau_p$ and t_p for long phases.

Figure S11a-j demonstrates consistent trends in the correlations for simulations with different numbers of particles, including correlations between $\Delta\tau$ and $g_{t10\%}D_{\min}^2$ across all instantaneous timesteps, between $\Delta\tau_p$ and both $mg_{t10\%}D_{\min}^2$ and $sg_{t10\%}D_{\min}^2$ for all, long, and short phases, and between $\Delta\tau_p$ and both mgD_{\min}^2 and sgD_{\min}^2 for long phases. Figure S11a-b and g shows that the correlations between $\Delta\tau_p$ and both $mg_{t10\%}D_{\min}^2$ and $sg_{t10\%}D_{\min}^2$ for the slip events ($\Delta\tau_p < 0$) across all phases mostly have stronger associations compared to those of $\Delta\tau$ with $g_{t10\%}D_{\min}^2$ across all instantaneous timesteps for the slip events ($\Delta\tau < 0$) in both simulations. These stronger correlations observed for all phases, rather than at individual timesteps, indicate that analyzing the microscopic dynamics over the duration of a phase provides a better understanding of the macroscale responses of granular materials in both simulations. Figure S11b-c and g-h shows that $\Delta\tau_p - mg_{t10\%}D_{\min}^2$ and $\Delta\tau_p - sg_{t10\%}D_{\min}^2$ in long phases not only follow the same trend as those observed in all phases but also are mostly more highly correlated during the slip events ($\Delta\tau_p < 0$) in both simulations. The correlations between $\Delta\tau_p$ and both $mg_{t10\%}D_{\min}^2$ and $sg_{t10\%}D_{\min}^2$ for long phases are strong for a significant decrease in $\Delta\tau_p$ ($\Delta\tau_p < -10^{-2}$) and mostly moderate for a small decrease in $\Delta\tau_p$ ($10^{-2} < \Delta\tau_p < 0$) in both simulations. On the other hand, Figure S11d and i indicates that $\Delta\tau_p$ and $mg_{t10\%}D_{\min}^2$, and $\Delta\tau_p$ and $sg_{t10\%}D_{\min}^2$, in short phases do not exhibit strong correlations across all $\Delta\tau_p$ regimes in both simulations. This can be attributed to the fluctuations during short phases as shown in Stage III of Figures 2b and S3b, particularly when the structure is unstable. Figure S11c, f, h, and j shows that the correlations between $\Delta\tau_p$ and both $mg_{t10\%}D_{\min}^2$ and $sg_{t10\%}D_{\min}^2$ for long phases are consistently stronger than those between $\Delta\tau_p$ and both mgD_{\min}^2 and sgD_{\min}^2 during slip events ($\Delta\tau_p < 0$), indicating that the variation in D_{\min}^2 values of particles around the one with the greatest D_{\min}^2 value has some effect on $\Delta\tau_p$ in both simulations. Figure S11e demonstrates that the partial correlations between $\Delta\tau_p$ and $mg_{t10\%}D_{\min}^2$ excluding the effect of gD_{\min}^2 for long phases in both simulations are moderate to strong for larger events ($\Delta\tau_p < -10^{-2}$), supporting our

previous argument that plastic events during these long slips are regional rather than point-like phenomena. Figure S11*c* and *h* shows that during the slip events ($\Delta\tau_p < 0$), the correlations between $\Delta\tau_p$ and $sg_{t10\%}D_{\min}^2$ are equal to or stronger than those between $\Delta\tau_p$ and $mg_{t10\%}D_{\min}^2$ in long phases in both simulations. This implies that the phenomenon is history-dependent in both simulations, given that $sg_{t10\%}D_{\min}^2$ represents the overall behavior of particle rearrangements during a slip event. Figure S11*k* illustrates varying trends in the correlation between $\Delta\tau_p$ and t_p for long phases in both simulations. The results show that $\Delta\tau_p$ and t_p are mostly moderately correlated for large $\Delta\tau_p$ values ($\Delta\tau_p > 10^{-4}$) in the long stick events in both simulations. Unlike in the slip events, the structure of a sample during the stick events remains stable, showing low gD_{\min}^2 values for long phases, and as a result, τ_p increases gradually with an increase in t_p . On the other hand, $\Delta\tau_p$ and t_p are weakly correlated during the slip events ($\Delta\tau_p < 0$) in long phases in both simulations because particle rearrangement is dominant during the long slip events.

Figure S12 presents the graphs for the same correlation analyses performed in Figure S2, which examined a smaller number of particles with various sliding friction coefficients, but now for a larger number of particles. The results show that the same trends were followed as in the case with a smaller number of particles in Figure S2. Here, employing a dataset that includes approximately 130,000 timesteps for each of the four simulations with sliding friction coefficients ($\mu_s = 0.1, 0.3, 0.5$, and 0.7), we observed approximately 12,000 phases for $\mu_s = 0.1$, 31,000 for $\mu_s = 0.3$, 31,000 for $\mu_s = 0.5$, and 26,000 for $\mu_s = 0.7$ within the steady-state regime (shear strain $\geq 5.4\%$).

In the simulation with a larger number of particles, compared to the simulation with a smaller number of particles, the number of minimum clusters in the GR region during a slip event, N_c , is generally greater (Figs. 5*c* and S10*c*). Therefore, we measured the absolute values of the Spearman correlation coefficients of $\Delta\tau_p$ with N_c across various ranges of $mg_{t10\%}D_{\min}^2$ and $sg_{t10\%}D_{\min}^2$, respectively, during long phases in the steady-state regime. (Fig. S13). The results show that these absolute correlation coefficients are weak, indicating that N_c does not influence $\Delta\tau_p$ regardless of the values of $mg_{t10\%}D_{\min}^2$ and $sg_{t10\%}D_{\min}^2$ during long phases in the steady-state regime.

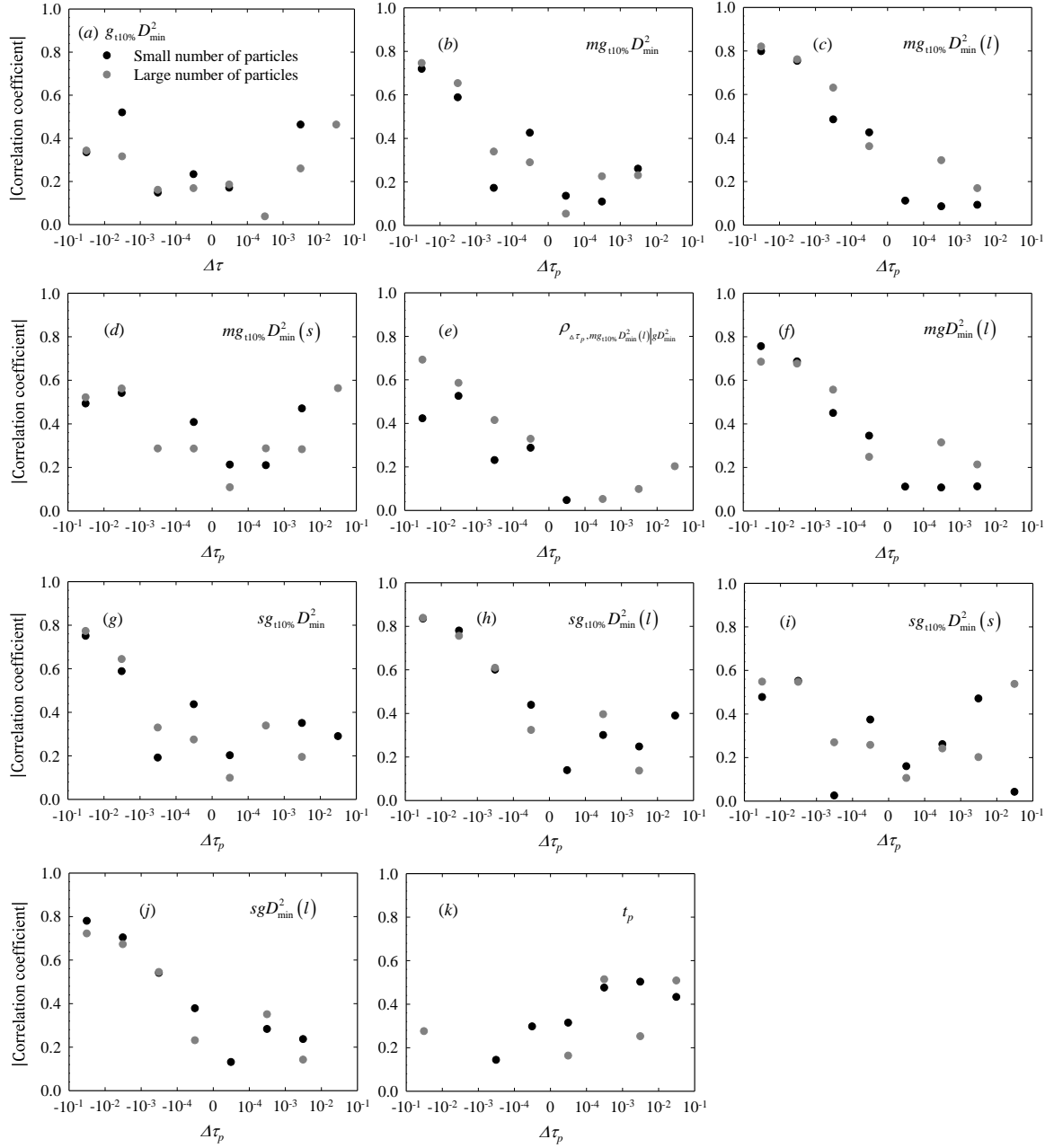


Fig. S11. Graphs of the absolute values of the Spearman correlation coefficients for between kinematic measures and $\Delta\tau$ or $\Delta\tau_p$ for simulations with a smaller number of particles in the stick-slip regime and a larger number of particles in the steady-state regime, with each represented by different colors, in the steady-state regime; (a) $\Delta\tau - g_{t10\%} D_{\min}^2$ across all instantaneous timesteps, (b) $\Delta\tau_p - mg_{t10\%} D_{\min}^2$ for all phases, (c) $\Delta\tau_p - mg_{t10\%} D_{\min}^2$ for long, l , ($> 3\Delta\gamma$) phases, (d) $\Delta\tau_p - mg_{t10\%} D_{\min}^2$ for short, s , ($\leq 3\Delta\gamma$) phases, (e) $\Delta\tau_p - mg_{t10\%} D_{\min}^2$ for long phases (partial correlation excluding the effect of $g D_{\min}^2$), (f) $\Delta\tau_p - mg D_{\min}^2$ for long phases, (g) $\Delta\tau_p - sg_{t10\%} D_{\min}^2$ for all phases, (h) $\Delta\tau_p - sg_{t10\%} D_{\min}^2$ for long phases, (i) $\Delta\tau_p - sg_{t10\%} D_{\min}^2$ for short phases, (j) $\Delta\tau_p - sg D_{\min}^2$ for long phases, and (k) $\Delta\tau_p - t_p$ for long phases.

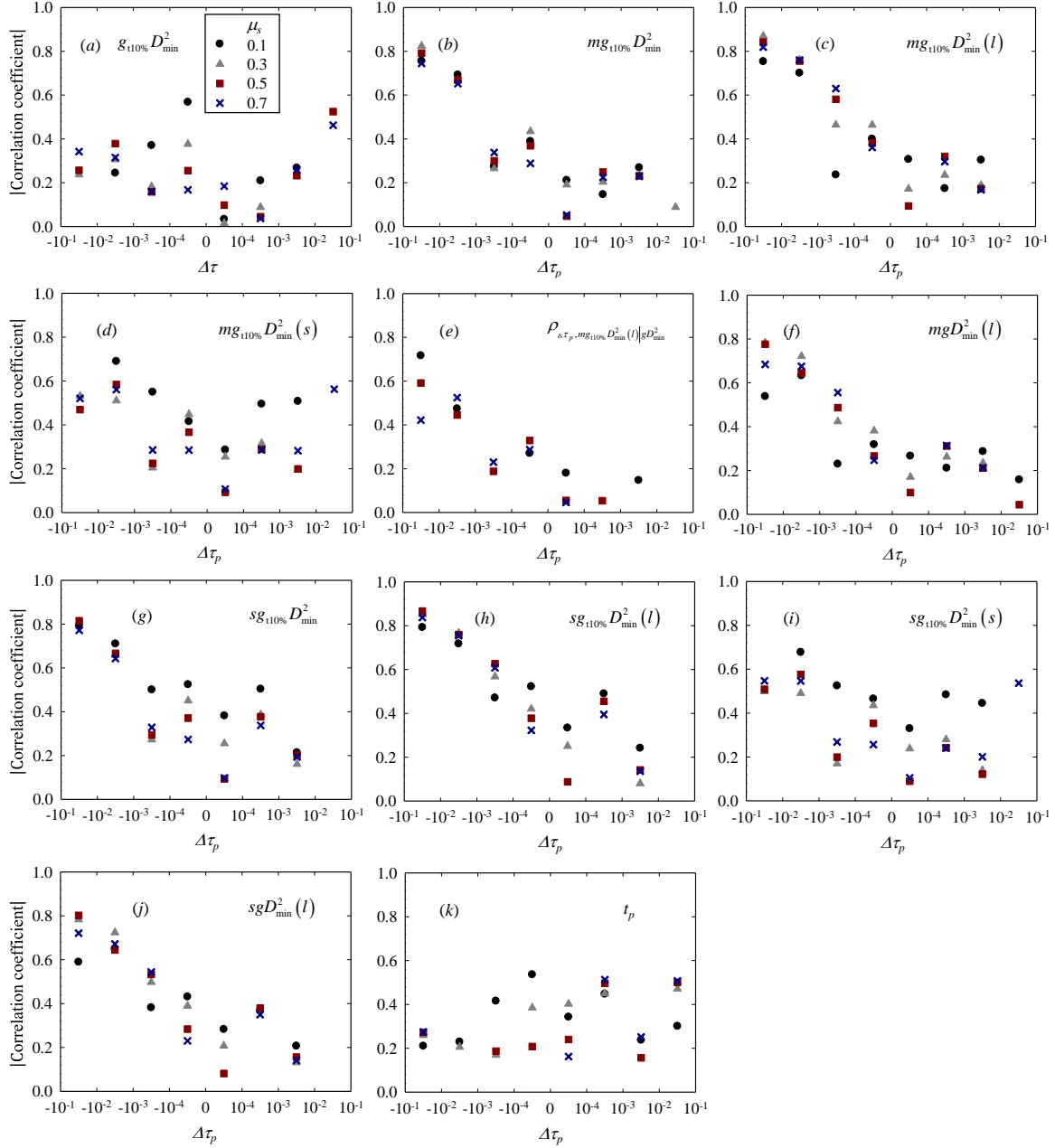


Fig. S12. Graphs of the absolute values of the Spearman correlation coefficients for between kinematic measures and $\Delta\tau$ or $\Delta\tau_p$ for various sliding friction coefficients, with each value of μ_s represented by different symbols, in the steady-state regime for the simulations with a large number of particles; (a) $\Delta\tau - g_{t10\%} D_{\min}^2$ across all instantaneous timesteps, (b) $\Delta\tau_p - mg_{t10\%} D_{\min}^2$ for all phases, (c) $\Delta\tau_p - mg_{t10\%} D_{\min}^2$ for long, l , ($> 3\Delta\gamma$) phases, (d) $\Delta\tau_p - mg_{t10\%} D_{\min}^2$ for short, s , ($\leq 3\Delta\gamma$) phases, (e) $\Delta\tau_p - mg_{t10\%} D_{\min}^2$ for long phases (partial correlation excluding the effect of gD_{\min}^2) (f) $\Delta\tau_p - mgD_{\min}^2$ for long phases, (g) $\Delta\tau_p - sg_{t10\%} D_{\min}^2$ for all phases, (h) $\Delta\tau_p - sg_{t10\%} D_{\min}^2$ for long phases, (i) $\Delta\tau_p - sg_{t10\%} D_{\min}^2$ for short phases, (j) $\Delta\tau_p - sgD_{\min}^2$ for long phases, and (k) $\Delta\tau_p - t_p$ for long phases.

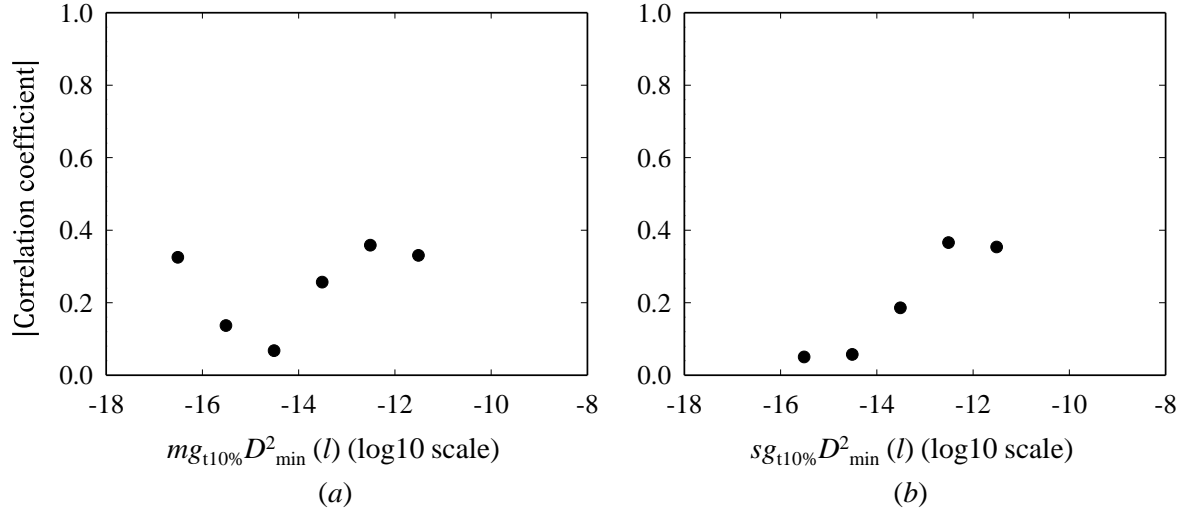


Fig. S13. The absolute values of the Spearman correlation coefficients between $\Delta\tau_p$ and with N_c across various ranges of (a) $mg_{t10\%} D_{\min}^2$ and (b) $sg_{t10\%} D_{\min}^2$, respectively, during long phases in the steady-state regime.